Master’s Thesis

Investigation into the prediction of the service life of the impeller of a turbo radial compressor in a high-temperature heat pump

M.Sc. in Power Engineering

Brandenburg University of Technology

In cooperation with

Institute of Low-Carbon Industrial Processes, German Aerospace Center (DLR)

Author

Name: Jonaed Bin Mustafa Kamal

Matriculation number: 4021457

Examiner

Prof. Dr.-Ing. Bernd Beirow

Head of the Chair of Structural Mechanics and Vehicle Vibrational Technology

BTU Cottbus-Senftenberg

Scientific supervisor

Martino Köhler

Scientific employee

Institute of Low-Carbon Industrial Processes

German Aerospace Center (DLR)

Date and place of submission: 23.08.2023, Cottbus

Declaration of authorship

I, Jonaed Bin Mustafa Kamal, hereby confirm that this thesis is entirely my own work and has not been submitted anywhere else. I am aware of the regulations of the Brandenburg University of Technology concerning plagiarism including the disciplinary actions associated with it. All the materials inside the thesis are acknowledged as appropriate.

______________________ ____________________

Place, Date Signature

Abstract

Out of all the components in a heat pump system, compressor is the one that is most prone to failure. For a compressor impeller to have a high lifetime, it is essential that it does not operate at any of its natural frequencies to avoid any resonance. Furthermore, the impeller rotates at speeds exceeding 100000 rpm and is subjected to alternating cycle load, and dynamic loads, e.g., centrifugal load, aerodynamic load, thermal load etc., resulting in cyclic stresses and further reducing the lifetime of the impeller. The maximum stresses occurring in an impeller must always be significantly lower than the yield point of the impeller material. This work predicts the number of cycles to failure of an impeller of a turbo-radial compressor for a high temperature heat pump by means of FEA using the strain-controlled fatigue analysis method. The stress analysis in the FEA is done using the von Mises criterion. A vibration analysis is done to find the dominant mode shape at the operating speed of the impeller and if there is any resonance.

Zusammenfassung

Von allen Komponenten eines Wärmepumpensystems ist der Verdichter diejenige, die erfahrungsgemäß die höchste Ausfallwahrscheinlichkeit hat. Für das Erreichen einer hohen Lebensdauer ist es wichtig, dass es nicht in einer seiner Eigenfrequenzen arbeitet, um Resonanzen zu vermeiden. Darüber hinaus dreht sich das Laufrad mit Drehzahlen von über 100000 U/min und ist wechselnden Zyklisch auftretenden Lasten und dynamischen Belastungen ausgesetzt, z. B. Zentrifugalkraft, aerodynamische Lasten, thermische Lasten etc., was zu zyklischen Belastungen führt und die Lebensdauer des Verdichter weiter verringert. Die in einem Laufrad auftretenden maximalen Spannungen müssen immer deutlich unter der Streckgrenze des Laufradmaterials liegen. In dieser Arbeit wird die Anzahl der Zyklen bis zum Versagen eines Laufrads eines Turboradialverdichters für eine Hochtemperaturwärmepumpe mittels FEA unter Verwendung der dehnungsgesteuerten Ermüdungsanalysemethode vorhergesagt. Die Spannungsanalyse in der FEA erfolgt nach dem von-Mises-Kriterium. Es wird weiterhin eine Schwingungsanalyse durchgeführt, um die dominante Modenform bei der Betriebsdrehzahl des Laufrads zu ermitteln und festzustellen, ob eine Resonanz vorliegt.

Acknowledgement

I would like to take this opportunity to thank the Department of High Temperature Heat Pump in the Institute of Low-Carbon Industrial Processes in the German Aerospace Center (DLR) for giving me the chance to write my Master’s thesis with them. I would like to express my sincere gratitude to Prof. Dr.-Ing. Bernd Beirow for taking the time to examine and review this thesis. I would like to thank my supervisor, Martino Köhler, without whose constant supervision, this thesis would not have been possible. I would also like to thank Nico Setzepfand, who helped me with the vibration section of this thesis. I am grateful to my friend Shampa, who was always by my side during this time. Finally, I would like to thank my parents and my sister for inspiring me at every moment of my life.

Table of contents

List of figures

List of tables

Nomenclature

Latin characters

Symbol	Designation	Unit
A	Area	m^2
B	Time scale parameter	-
b	Fatigue strength exponent	-
c	Fatigue ductility exponent	-
$[D]$	Damping matrix	Ns/m
E	Modulus of elasticity	Pa
EO	Engine order	-
F	Force	N
F_i	Force along i direction ($i = x, y, z$)	N
f	Frequency	Hz
H	Cyclic strength coefficient	Pa
i	Blade position	-
$[K]$	Stiffness matrix	N/m
$[M]$	Mas matrix	kg
m	Integer greater than or equal to 0	-
N_b	Number of blades	-
N_f	Number of cycles to failure	-
ND	Number of nodal diameters	-
ND_max	Maximum number of nodal diameters	-
n	Strain hardening exponent	-
q	Modal displacement	m
R	Stress ratio	-
RPM	Revolutions per minute	rpm
r	Radial distance	m
t	Time	s
x	Displacement / displacement along x direction	m
$\ddot{x}$	Acceleration	m/s^2
$\dot{x}$	Velocity	m/s
y	Displacement along y direction	m
$y_\mathrm{1,glob}, z_\mathrm{1,glob}$	y and z coordinates of the first point in the global coordinate system	-
y_1, z_1	y and z coordinates of the first point in the local coordinate system	-
$y_\mathrm{n,glob}, z_\mathrm{n,glob}$	y and z coordinates of the nth point in the global coordinate system	-
$y_\mathrm{n}, z_\mathrm{n}$	y and z coordinates of the nth point in the local coordinate system	-
z	Displacement along z direction	m

Greek characters

Symbol	Designation	Unit
α	angle between the horizontal line through the origin of the local coordinate system and the line connecting the point and the origin	°
α_{n}	Angle between the horizontal line through the origin of the local coordinate system and the nth point	°
ε	Strain	m/m
$\Delta\varepsilon_{\mathrm{e}}$	Elastic strain range	m/m
$\Delta\varepsilon_{\mathrm{p}}$	Plastic strain range	m/m
$\Delta\varepsilon$	Strain range	m/m
ε_{f}	Strain at rupture point	m/m
$\varepsilon_{\mathrm{f}}'$	Fatigue ductility coefficient	Pa
ε_{i}	Strain along i direction ($i = x, y, z$)	m/m
ε_{u}	Strain at ultimate point	m/m
ε_{y}	Strain at yield point	m/m
$\Delta\theta$	Angular difference	°
σ	Stress	Pa
$\Delta\sigma$	Stress range	Pa
σ_{a}	Stress amplitude	Pa
σ_{e}	Fatigue limit	Pa
σ_{f}'	Fatigue strength coefficient	Pa
σ_{m}	Mean stress	Pa
σ_{max}	Maximum stress	Pa
σ_{min}	Minimum stress	Pa
σ_{u}	Ultimate stress	Pa
σ_{VM}	Von Mises stress	Pa
σ_{y}	Yield stress	Pa
σ_{i}	Normal stress along i direction ($i = x, y, z$)	Pa
σ_{k}	Principal stress ($k = 1,2,3$)	Pa
τ_{ij}	Sheer stress on the ij plane ($ij = xy, yz, zx, yx, zy, xz$)	Pa
ω	Rotational speed	rad/s
ω_{n}	Natural frequency	Hz
ϕ_{j}	Eigenvector	-
ϕ_{IBPD}	Inter-blade phase difference	rad
λ	Eigenvalue	-
ν	Poisson’s ratio	-

Abbreviations

Abbreviation	Designation
CAD	Computer aided design
FEA	Finite element analysis
HCF	High cycle fatigue
LCF	Low cycle fatigue
ZZENF	Zig-zag shaped excitation line in the nodal diameter versus frequency

1 Introduction

The Paris Agreement at UN Climate Change Conference (COP21) in 2015 set the goal of limiting the increase in the global average temperature to 1.5° C above pre-industrial levels [1]. This ambitious goal, otherwise known as the 1.5° pathway, requires extensive change in energy production and consumption practices. In order to meet this goal and to have a net-zero emission by 2050, an annual cut of 37 Gt of CO_2 is necessary with an increase in the share of renewable energy to 79% [2]. The International Renewable Energy Agency (IRENA) identifies six technological avenues towards achieving this goal. Out of these avenues, electrification by means of clean electricity and increasing energy efficiency are distinguished as two major components. Decarbonizing by electrification mostly refers to use of clean energy in the transport and heating sectors [2]. Decarbonization of heating in the industrial sector will play a vital role in the reduction of global greenhouse gas (GHG) emission. The industrial sector is responsible for 32% of the total GHG emissions [3]. In the European Union (EU) the industrial energy consumption amounts to about 3200 TWh per year, with 70% of it being consumption of heat and the rest electricity. Industrial heat consumption in the EU can be categorized into process heating and space heating. Furthermore, industrial process heat can be divided into high temperature process heat (above 200° C) and low temperature process heat (below 200° C) [4]. The production of this industrial heat is mostly covered by the use of fossil fuel [5]. Changes in the process operation of energy intensive industries through increase in efficiency of industrial processes, waste heat utilization, and transition of energy sources from fossil fuel to renewable sources can reduce the global GHG emissions by 80% by 2050 [3, 6, 7].

Industrial heat pump is a promising technology in increasing the efficiencies of industrial processes by means of waste heat utilization, while integration of renewable energy with heat pumps can further reduce CO_2 emission in the industrial sector. Kosmadakis [8] gives an estimation of the potential of heat pumps in the exploitation of waste heat in the EU. He estimates that the use of industrial heat pump has the potential to cover a significant amount of the heat consumption of industries like non-ferrous metal, chemical, non-metallic mineral, food and tobacco, and paper and pulp industries. Furthermore, it is shown that, in the EU, industrial heat pump with a coefficient of performance (COP) of 4 has the potential to cover 28.37 TWh of industrial heat consumption per year, which is about 15% of the heat consumption by processes operating between 100° C to 200° C and 1.5% of the total industrial heat consumption. In a separate study, Marina et al. [3] give an estimation of the total process heat that can be covered by industrial heat pumps, and the associated energy and CO_2 saving potential in four sectors, i.e., food, paper, chemical and refinery sectors. They show that, in the aforementioned four sectors, the current heat pump market has the potential to cover 547 PJ/year or about 73% of the total heat consumption for applications up to 150° C and 641 PJ/year or about 57% of the total heat consumption for applications up to 200° C. In the current energy scenario, this would reduce the final energy consumption in these four sectors by about 313 PJ/year, which is equivalent to about 371 PJ/year of fossil fuel avoided, resulting in a CO_2 emission reduction of 37.3 Mt/year. In a scenario with 100% renewable electricity, the reduction in final energy consumption amounts to 528 PJ/year or 724 PJ/year of fossil fuel avoided, which could lower the CO_2 emission by 52.6 Mt/year.

When working with heat pump components, it is necessary to understand the working principle of a heat pump. Heat pumps can be classified into vapor compression heat pumps and absorption heat pumps. A vapor compression heat pump follows a reverse thermodynamic cycle by using a mechanical compressor driven by an electric motor or an engine. Absorption heat pumps use a mixture of two fluids having different vapor pressures. Since the focus of this work is on the development of a centrifugal compressor for a vapor compression heat pump, only this technology is referred from now on.

A vapor compression heat pump has four main components in its simplest configuration. As shown in Figure 1-1, a heat pump has a compressor driven by a motor, a heat exchanger working as a condenser, an expansion valve, and another heat exchanger that works as an evaporator. The compressor maintains the right pressure drop between the condenser and the evaporator. The superheated vapor coming from the compressor is de-superheated and condensed in the condenser. The pressure of the condensed liquid is then irreversibly taken to the pressure of the evaporator in the expansion valve. The mixture coming from the expansion valve is then saturated or superheated inside the evaporator before it is passed back on to the compressor. To characterize a heat pump, a parameter known as coefficient of performance (COP) is used. COP is the ratio of the total heat extracted from the heat pump to the work supplied to the heat pump [9].

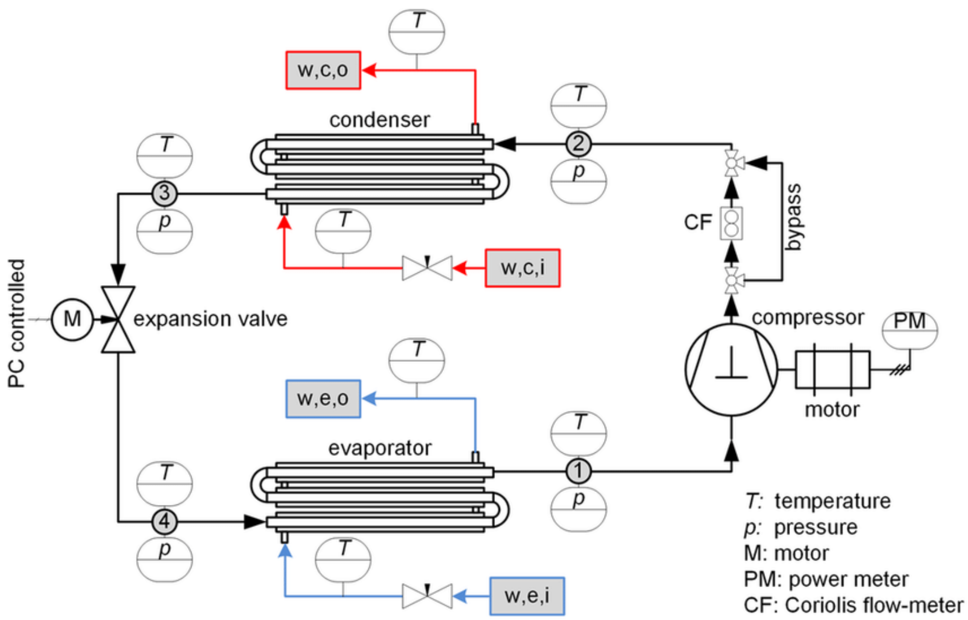

Figure 1-1: Flow diagram of a heat pump showing different components and sensors [10]

Out of all the components (including primary and secondary components) of a heat pump system, compressor is the one that is most prone to failure. In a case study performed by Aguilera et al. [11], it was seen that, out of a total of 129 faults in different heat pumps, 25% were attributed to compressors. The most frequent cause behind these failures was identified as excessive noise and vibration. Excessive vibration of a rotating compressor has a direct effect on the lifetime of the compressor, as well as other components, e.g., gears, bearings, and valves [11]. Failure occurs when the excitation frequency is close to the natural frequency of the component, causing resonance. To have a high life time of the compressor, resonance should be avoided at the operating speed of the compressor [12]. Additionally, a centrifugal compressor is a device that rotates at speeds exceeding 100000 rpm and is subjected to alternating cycle load, and dynamic loads, e.g., centrifugal load, aerodynamic load, exciting load, thermal load and so on. Furthermore, the compressor is also exposed to collisions from particles in the medium. These loads result in different failure modes that include stress fatigue, abrasion, and erosion resulting in fatigue cracking and fracture of the compressor [13]. This thesis predicts the service life of a centrifugal compressor for a high temperature heat pump, developed by the Institute of Low-Carbon Industrial Processes of the German Aerospace Center (DLR) as part of a pilot project, by calculating the number of cycles to failure using a strain-based approach. A vibration analysis is also done on the impeller.

2 Theoretical Framework

2.1 Fundamentals of stress and strain

Stress is defined as the internal resistance of a body if a force is applied to it. It is measured as load per unit area of the surface that the force is acting upon and can be expressed by equation 2.1.

$$\sigma = \frac{F}{A} \tag{2.1}$$

where, F is the force and A is the area of the surface on which the force is applied.

The stress acting normal to the surface is known as normal stress. Depending upon the direction of the stress with respect to the surface, the normal stress can be tensile or compressive. The stress acting parallel to the surface is known as sheer stress [14, 15].

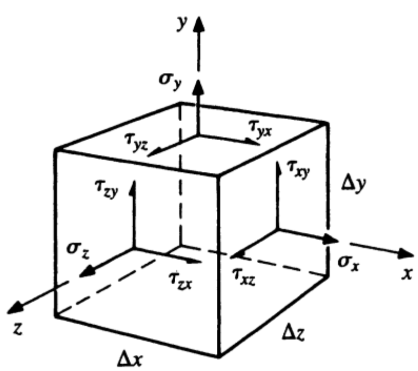

Figure 2-1: Components of a stress acting on the three orthogonal surfaces

The force, F, will have components F_{x}, F_{y} and F_{z} in the x, y and z direction of a defined Cartesian coordinate system, and associated normal stresses σ_{x}, σ_{y} and σ_{z}. The sheer stresses acting on the different planes will be τ_{xy}, τ_{yx} τ_{yz}, τ_{zy}, τ_{zx} and τ_{xz} (see Figure 2-1). Thus, the complete stress tensor can then be written as equation 2.2 [15, 16].

$$\sigma = \begin{bmatrix} \sigma_{\mathrm{x}} & \tau_{xy} & \tau_{\mathrm{xz}} \\ \tau_{yx} & \sigma_{\mathrm{y}} & \tau_{\mathrm{yz}} \\ \tau_{\mathrm{zx}} & \tau_{\mathrm{zy}} & \sigma_{\mathrm{z}} \end{bmatrix} \tag{2.2}$$

The normal stresses are maximum or minimum on surfaces where the sheer stresses are zero. These stresses are known as principal stresses and are the eigenvalues of the stress matrix. The associated planes are called the principal planes. The three principal stresses, denoted as σ_1, σ_2 and σ_3, are ordered in such a way that $\sigma_1 \geq \sigma_2 \geq \sigma_3$ [15].

Strain is a measure of the distortion of an object due to stress. Similar to stress, there are two types of strain, i.e., normal strain and sheer strain. Normal strain is defined as the change in length of an element subjected to the associated normal stress divided by the original length of the element.

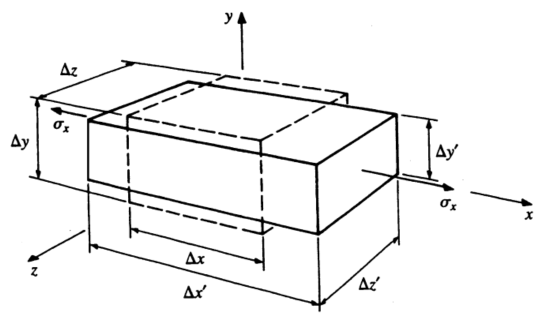

Figure 2-2: Deformation of an element subjected to a stress, σ_x [15]

If an element changes its shape as seen in Figure 2-2, the strains along the x, y and z directions are defined as equations 2.3, 2.4 and 2.5 [15, 16].

$$\varepsilon_x = \frac{\Delta x' - \Delta x}{\Delta x} \tag{2.3}$$

$$\varepsilon_y = \frac{\Delta y' - \Delta y}{\Delta y} \tag{2.4}$$

$$\varepsilon_z = \frac{\Delta z' - \Delta z}{\Delta z} \tag{2.5}$$

Hooke's law says that, within the elastic limit, for a linear, homogeneous and isotropic material, the normal stress, σ, is directly proportional to the normal strain, ε, and can be shown by equation 2.6 [17],

$$\sigma = E\varepsilon \tag{2.6}$$

The proportionality constant, E, in equation 2.6 is known as the modulus of elasticity or Young's modulus and is a material property. E is a measure of the stiffness of a material under tension or compression. A material in tension has an axial strain, as well as lateral strains that are perpendicular and proportional to the axial strain. If a stress has the components σ_{x}, σ_{y} and σ_{z}, the corresponding strains ε_{x}, ε_{y} and ε_{z} can be expressed by equations 2.7, 2.8 and 2.9 [15, 17].

$$\varepsilon_{\mathrm{x}} = \frac{1}{E}\left[\sigma_{\mathrm{x}} - \nu\left(\sigma_{\mathrm{y}} + \sigma_{\mathrm{z}}\right)\right] \tag{2.7}$$

$$\varepsilon_{\mathrm{y}} = \frac{1}{E}\left[\sigma_{\mathrm{y}} - \nu(\sigma_{\mathrm{z}} + \sigma_{\mathrm{x}})\right] \tag{2.8}$$

$$\varepsilon_{\mathrm{z}} = \frac{1}{E}\left[\sigma_{\mathrm{z}} - \nu\left(\sigma_{\mathrm{x}} + \sigma_{\mathrm{y}}\right)\right] \tag{2.9}$$

The proportionality constant, ν, is known as the Poisson's ratio and is the ratio of a material's lateral strain to its longitudinal strain [15, 16].

The relationship between normal stress and normal strain can be further explained by a tensile stress-strain curve, shown in Figure 2-3.

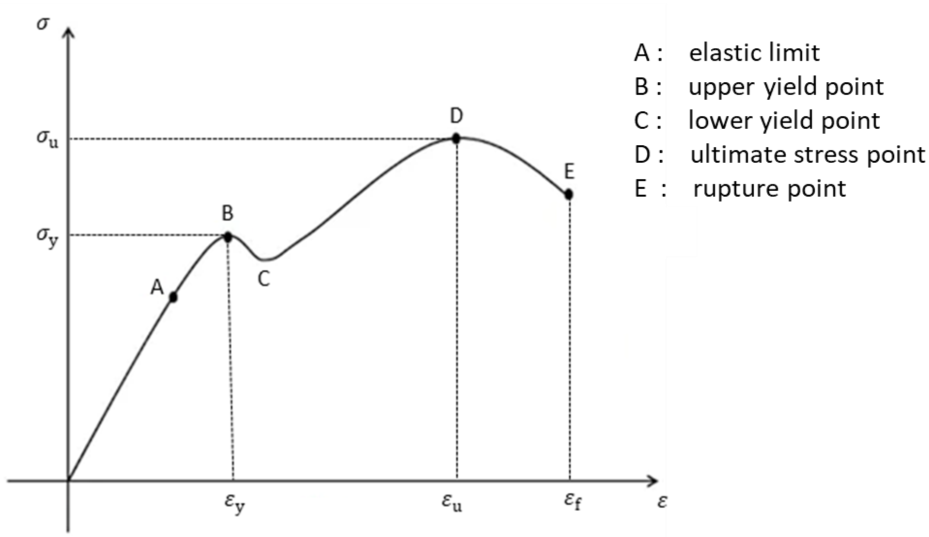

Figure 2-3: Tensile stress-strain curve. σ_{y} and σ_{u} represent yield stress and ultimate stress. ε_{y}, ε_{u} and ε_{f} represent strains at yield point, ultimate stress point and rupture point.

The stress in Figure 2-3 is the engineering stress. Contrast to the true stress, defined as load divided by the actual area, the engineering stress refers to load divided by the initial area. Linear elastic deformation occurs until point A. This point is known as the elastic limit. Until this point, the tensile stress is proportional to the strain (see equation 2.6). After point B, there is permanent plastic deformation. This point is known as the yield point. The stress at this point is known as the yield stress, which is a property of the material, and is denoted by σ_{y}. In some materials, e.g., low carbon steels, the amount of stress required to initiate the plastic deformation is higher than the stress required to hold it, resulting in an upper yield point and a lower yield point. Point B and point C represent the upper and lower yield points. Following these points, the stress, required for deformation keeps increasing until point D. This point is known as the ultimate stress point and the stress at this point is known as the ultimate stress, denoted by σ_{u}. This is also known as the ultimate strength of a material and is a mechanical property of the material. After this point, the stress decreases with increasing strain and non-uniform deformation of the material takes place. This is known as necking. At point E or the rupture point, fracture occurs at a strain ε_{f} [18].

2.2 Criteria for elastic failures

Elastic failure occurs in a ductile material when the material undergoes marked plastic deformation. The six theories that are used to describe elastic failure are the maximum principal stress theory, the maximum sheer stress theory, the maximum principal strain theory, the maximum strain energy theory, the maximum distortion energy theory, and the maximum octahedral sheer stress theory. Out of these theories, for ductile materials, the maximum distortion energy theory and the maximum octahedral sheer stress theory agree the most with experiments [15]. The stress analysis in this thesis is done based on the maximum distortion energy theory.

The maximum distortion energy theory, also known as the von Mises stress theory, states that elastic failure occurs when the energy of distortion becomes equal to the energy of failure in tension. The state of stress at this point is described by the right side of equation 2.10. This equivalent stress is known as the von Mises stress and is denoted by σ_{VM} [15, 16]. Elastic failure occurs when σ_{VM} reaches σ_{y}.

$$\sigma_{\mathrm{VM}} = \sqrt{\frac{1}{2}[(\sigma_1 - \sigma_2)^2 + (\sigma_2 - \sigma_3)^2 + (\sigma_3 - \sigma_1)^2]} \tag{2.10}$$

When written in terms of the normal and sheer stresses instead of the principal stresses, σ_{VM} can be expressed by equation 2.11 (for the details about principal, normal and sheer stresses, see section 2.1).

$$\sigma_{\mathrm{VM}} = \sqrt{\frac{1}{2}[(\sigma_{\mathrm{x}} - \sigma_{\mathrm{y}})^2 + (\sigma_{\mathrm{y}} - \sigma_{\mathrm{z}})^2 + (\sigma_{\mathrm{z}} - \sigma_{\mathrm{x}})^2 + 6({\tau_{\mathrm{xy}}}^2 + {\tau_{\mathrm{yz}}}^2 + {\tau_{\mathrm{zx}}}^2)]} \tag{2.11}$$

2.3 Mechanical properties of a material

The most important mechanical properties of a material include modulus of elasticity or Young's modulus, yield strength, ultimate tensile strength, fatigue limit, Poisson's ratio and Brinell hardness. All of these properties except the Brinell hardness are discussed in detail in section 2.1. The Brinell hardness test is done to test the hardness of a material and is performed by causing an indentation on the material using a specified load (usually 3000 kg). The result of the test is expressed by a number known as the HB number. A higher HB number denotes a higher hardness of the material [18].

2.4 Fatigue life of a material

As has been discussed in section 2.2, the maximum allowable von Mises stress must not exceed the yield point of the material. To avoid any plastic deformation of a component it is essential that the stress due to loading is well below the yield point (point B in the stress-strain diagram shown in Figure 2-3). However, even when the component works under a stress that is below the yield point or not enough to cause immediate rupture, repetitive stress causes the component to fail after a certain number of cycles. This number of cycles is known as the fatigue life of the component. When the stress that the component goes through is in the elastic region, fatigue life is related to the total stress and eventually strain, since strain is directly proportional to stress in the elastic region. Beyond the elastic region, fatigue life can only be related to the total strain, i.e., sum of elastic and plastic strains, and not the stress. The relation between the total strain and the number of cycles can be visualized by a curve known as the S-N curve or Wöhler curve (see Figure 2-4). The fatigue life of a component can be characterized using a stress-based approach when the stress is within the elastic limit. However, to see the effect of any plasticity, a strain-based approach is necessary, since a strain-based calculation takes into account both the elastic and the plastic parts of the strain. This thesis characterizes the fatigue life of a compressor for a high temperature heat pump using a strain-based approach. The following sections describe the different modes of fatigue, the relation between strain and number of cycles to failure, and the governing equations used in a strain-based fatigue life calculation.

2.4.1 High cycle fatigue (HCF) and low cycle fatigue (LCF)

Cycle fatigue in materials can be attributed to two conditions. The first condition is known as the cyclic stress-controlled fatigue. The stresses in this condition remain below the yield stress and generally remain elastic. An example of this case is the alternating stress associated with a rotating object, e.g., a shaft. Fatigue in this case occurs after a high number of load cycles. For this reason, this is also known as high cycle fatigue (HCF).

The second condition is known as the cyclic strain-controlled fatigue. This mostly occurs as a result of geometric stresses, e.g., stresses due to the presence of a notch, or material imperfections. Cyclic strain-controlled fatigue leads to localized plastic deformation. As a result, failure occurs after a low number of load cycles. This phenomenon is also known as low cycle fatigue (LCF) [14, 19].

In the following sections, the terms HCF and LCF will be used instead of cyclic stress-controlled fatigue and cyclic strain-controlled fatigue.

2.4.2 S-N curve

One of the commonly used methods to determine the fatigue life of a material is the S-N curve (shown in Figure 2-4). The stress amplitude or the strain amplitude is plotted as a function of cycles to failure. The S-N curve is an expression of fatigue strength of a material after a certain number of cycles. For ferrous and titanium alloys, there is a limit to the stress amplitude below which the material can exhibit an infinitely large number of cycles to failure. This is known as the endurance limit or fatigue limit and is denoted by σ_{e}. For other non-ferrous materials, no such limit occurs. Thus, an arbitrarily chosen large number of cycles is used to characterize the limits for these materials [20].

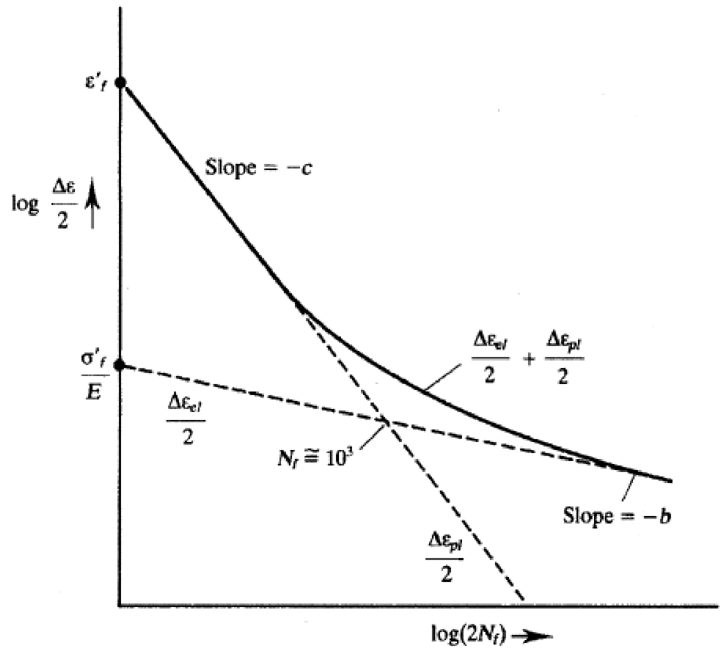

Figure 2-4: S-N curve plotted in terms of stress amplitude [18]

When plotted, the curve can be divided into two areas. The left side of the curve gives the LCF part that has a stress amplitude higher than the endurance limit and can be described by Coffin's law, while the right side of the curve gives us the HCF part, which has a stress amplitude lower than the endurance limit and can be described by Basquin's law. A detailed description of these phenomena is given in section 2.4.3.

2.4.3 Governing equations in fatigue life analysis

The key definitions of stress, in describing the fatigue life, for an alternating stress between a maximum stress of $\sigma_{\max}$ and a minimum stress of $\sigma_{\min}$ are shown in Figure 2-5 and given by equations 2.12, 2.13, 2.14 and 2.15 [14, 19].

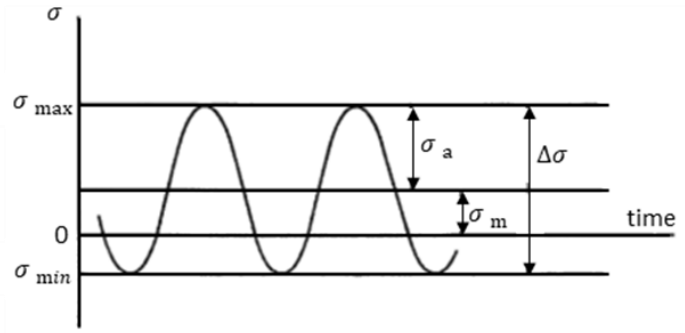

Figure 2-5: Alternating stress between a maximum and a minimum stress value [19]

$$\Delta\sigma = \sigma_{\mathrm{max}} - \sigma_{\mathrm{min}} \tag{2.12}$$

$$\sigma_{\mathrm{a}} = \frac{\Delta\sigma}{2} = \frac{\sigma_{\mathrm{max}} - \sigma_{\mathrm{min}}}{2} \tag{2.13}$$

$$\sigma_{\mathrm{m}} = \frac{\sigma_{\mathrm{max}} + \sigma_{\mathrm{min}}}{2} \tag{2.14}$$

$$R = \frac{\sigma_{\mathrm{min}}}{\sigma_{\mathrm{max}}} \tag{2.15}$$

Here, $\Delta\sigma$, σ_{a}, σ_{m} and R are the stress range, stress amplitude, mean stress and the stress ratio respectively.

In order to calculate the total strain of a material under cyclic loading, the elastic and the plastic components of the strain have to be calculated separately. The elastic component of strain or the HCF part of the S-N curve, shown in Figure 2-4, can be described using the so called Basquin's equation, given by equation 2.16. Basquin's equation relates the stress amplitude to the number of cycles to failure, N_{f} [14].

$$\sigma_{\mathrm{a}} = \sigma_{\mathrm{f}}'(2N_{\mathrm{f}})^{b} \tag{2.16}$$

σ_{f}' is a material property known as the fatigue strength coefficient and b is known as the fatigue strength exponent. An increasing σ_{f}' and a decreasing b result in an increasing N_{f}.

The validity of the Basquin's law can be extended to describe the dependence of fatigue limit of finite life on the number of cycles to fatigue using the Palmgren function. The Palmgren function, expressed by equation 2.17, applies to both the low cycle and the high cycle part of the S-N curve [21].

$$\sigma = \sigma_f{}'(N_f + B)^b + \sigma_e \tag{2.17}$$

Here, B is known as the time scale parameter and σ_e is the fatigue limit of the material. The value of B for Ti-6Al-4V, which is the used material in this thesis, is 4900 [21]. σ_e for Ti-6Al-4V is taken from the material data sheet given by the manufacturer of the impeller used in this thesis and has a value of 240 MPa. The Palmgren function can be used to calculate stress at any N_f for a material, thus giving the S-N curve of the material in both the HCF (>10^4 cycles) and the LCF (<10^4 cycles) region. The S-N curve of the material, Ti-6Al-4V, is found using this function and is shown in Figure 2-6.

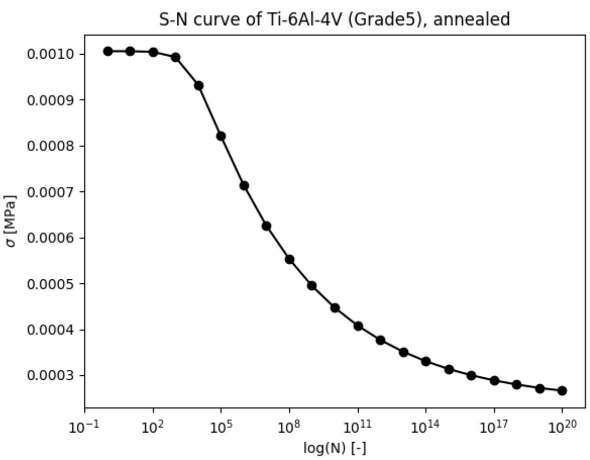

Figure 2-6: S-N curve of Ti-6Al-4V, calculated using the Palmgren function, given by equation 2.17

In the elastic region, as per Hooke's law, the strain amplitude, $\frac{\Delta\varepsilon_e}{2}$, can be calculated using equation 2.18 (see equation 2.6) [19].

$$\frac{\Delta\varepsilon_e}{2} = \frac{\sigma_a}{E} = \frac{\sigma_f{}'}{E}(2N_f)^b \tag{2.18}$$

The plastic component of strain or the LCF part of the S-N curve, presented in Figure 2-4, is described by Coffin's law, given by equation 2.19 [19].

$$\frac{\Delta\varepsilon_{\mathrm{p}}}{2} = \varepsilon_{\mathrm{f}}'(2N_{\mathrm{f}})^{c} \tag{2.19}$$

$\varepsilon_{\mathrm{f}}'$ is known as the fatigue ductility coefficient and c is known as the fatigue ductility exponent.

The superposition of the elastic and plastic strain amplitude gives the total strain amplitude, $\frac{\Delta\varepsilon}{2}$, given by equation 2.20 [19, 22]. This equation is most commonly known as the Manson-Coffin relation.

$$\frac{\Delta\varepsilon}{2} = \frac{\Delta\varepsilon_{\mathrm{e}}}{2} + \frac{\Delta\varepsilon_{\mathrm{p}}}{2} = \frac{\sigma_{\mathrm{f}}'}{E}(2N_{\mathrm{f}})^{b} + \varepsilon_{\mathrm{f}}'(2N_{\mathrm{f}})^{c} \tag{2.20}$$

The effect of compressive and tensile mean stress, σ_{m}, can be included by modifying equation 2.20 to equation 2.21. Studies show that equation 2.21 fits reasonably well with fully reversed and mean stress data [22].

$$\frac{\Delta\varepsilon}{2} = \frac{\Delta\varepsilon_{\mathrm{e}}}{2} + \frac{\Delta\varepsilon_{\mathrm{p}}}{2} = \frac{\sigma_{\mathrm{f}}' - \sigma_{\mathrm{m}}}{E}(2N_{\mathrm{f}})^{b} + \varepsilon_{\mathrm{f}}'(2N_{\mathrm{f}})^{c} \tag{2.21}$$

Zhao et al. [23] presents a number of methods for calculating σ_{f}' and ε_f' for steel based alloys. These methods include the modified universal slopes method [24], universal material law [25], and hardness method [26]. Sharifimehr et al. [27] presents a modified version of the equation given in [26] to calculate σ_{f}' and $\varepsilon_{\mathrm{f}}'$ for titanium based alloys. Since the material used in this thesis is a Ti based alloy, namely, Ti-6Al-4V, the method presented in [27] is chosen to calculate σ_{f}' and $\varepsilon_{\mathrm{f}}'$. The equations to calculate σ_{f}' and $\varepsilon_{\mathrm{f}}'$ of titanium based alloys (HB between 240 and 353) are given by equations 2.22 and 2.23 [27].

$$\sigma_{\mathrm{f}}' = 4.25(HB) + 225 \text{ MPa} \tag{2.22}$$

$$\varepsilon_{\mathrm{f}}' = \frac{[430000 - 44(HB)}{E} \text{ MPa} \tag{2.23}$$

The values of b and c are taken as -0.09 and -0.56 in this method [27].

For metals, the relationship between stress and strain in the plastic region fits a power relationship, expressed by equation 2.24 [28].

$$\varepsilon_{\mathrm{p}} = \left(\frac{\sigma}{H}\right)^{\frac{1}{n}} \tag{2.24}$$

When the cyclic stress-strain diagram is plotted in a log-log plot, equation 2.24 gives a straight line that has a slope of n. This value, n, is known as the strain hardening exponent and is a measure of the rate of strain hardening that the material goes through after the yield point. A higher n means the material is likely to go through strain hardening, while a lower n means the material is likely to go through strain softening. For metals, the value of n is in the range of 0.1 to 0.2. The other quantity, H, is known as the cyclic strength coefficient and is a measure of the stress magnitude in a cyclic stress-strain plot [28].

The elastic strain can be found by Hooke's law using equation 2.6. The total strain, ε, thus can be found by adding ε_{e} and ε_{p} (shown in equation 2.25). This equation is known as the Ramberg-Osgood relationship [28].

$$\varepsilon = \varepsilon_{\mathrm{e}} + \varepsilon_{\mathrm{p}} = \frac{\sigma}{E} + \left(\frac{\sigma_{\mathrm{a}}}{H}\right)^{\frac{1}{n}} \tag{2.25}$$

Equation 2.24 can be used to calculate the values of n and H from the stress and strain values of two known points, e.g., the ultimate and the yield point. This is shown by equations 2.26 and 2.27.

$$n = \frac{\log\left(\frac{\sigma_{\mathrm{u}}}{\sigma_{\mathrm{y}}}\right)}{\log\left(\frac{\varepsilon_{\mathrm{u}}}{\varepsilon_{\mathrm{y}}}\right)} \tag{2.26}$$

$$H = \frac{\sigma_{\mathrm{y}}}{{\varepsilon_{\mathrm{y}}}^{n}} \tag{2.27}$$

The yield point is typically defined using the 0.2% offset method, where σ_{y} is determined to be the stress at which the material is plastically strained by 0.2% strain offset. Thus, in this method, the strain at yield point, ε_{y}, is 0.002 [29]. Putting this value in equation 2.27 and replacing H in equation 2.25, the total strain amplitude can be calculated from equation 2.28.

$$\frac{\Delta\varepsilon}{2} = \frac{\sigma_{\mathrm{a}}}{Y} + 0.002\left(\frac{\sigma_{\mathrm{a}}}{\sigma_{\mathrm{y}}}\right)^{\frac{1}{n}} \tag{2.28}$$

2.5 Vibration analysis of an impeller

The impeller of a compressor is a mechanical system of multi-degree of freedom. The equation of motion for a multi-degree of freedom mechanical system acting under an excitation force, F_{A}, can be expressed by the differential equation 2.29 [30, 31].

$$[M]\ddot{x} + [D]\dot{x} + [K]x = F_{\mathrm{A}} \tag{2.29}$$

Here, $[M]$, $[D]$ and $[K]$ are called the mass matrix, the damping matrix, and the stiffness matrix respectively.

The first step of a vibration analysis is to find a solution to equation 2.29 for an unloaded and undamped system. The vibration in this case is known as free vibration and the analysis is called a modal analysis. For an unloaded and undamped system, equation 2.29 becomes,

$$[M]\ddot{x} + [K]x = 0 \tag{2.30}$$

Thus, the model, represented by equation 2.30, only depends on the mass and elastic properties of the system. The solution to equation 2.30 contains the eigenvectors, ϕ_{j}, of the unloaded and undamped system [31].

$$x(t) = \phi_{\mathrm{j}} e^{\lambda t} \tag{2.31}$$

From this eigenvalue problem, the eigenvector, ϕ_{j}, and the eigenvalue, λ, can be determined. The natural frequency, ω_{n}, is the square root of λ. ϕ_{j} represents the mode shape [30].

$$\lambda = {\omega_{\mathrm{n}}}^2 \tag{2.32}$$

A mode shape of a disk is characterized by its nodal diameters and nodal circles. The nodal diameter is the line where the structure does not undergo any deflection, and which separates two adjacent areas with opposite vibration. Similarly, the structure does not experience any deflection in the position of the nodal circle. Figure 2-7 shows different mode shapes with different number of nodal diameters and nodal circles.

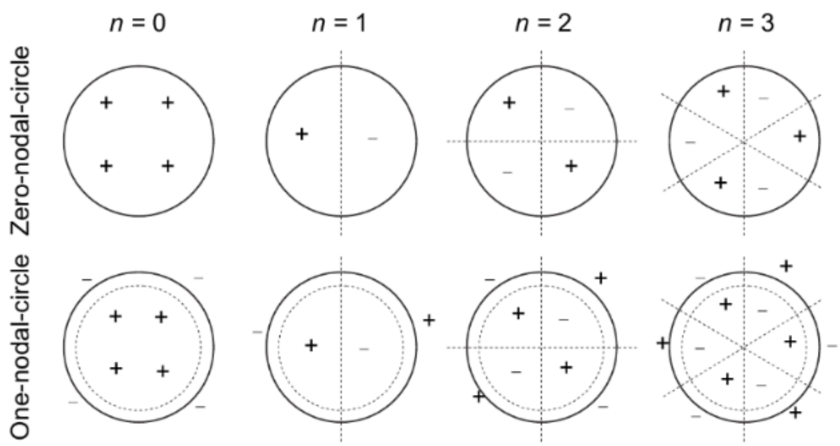

Figure 2-7: Mode shapes with different number of nodal lines and nodal circles [32]

The maximum number of nodal diameters, ND_{max}, depends on the number of blades, N_{b}, and can be expressed by equations 2.33 and 2.34 [31, 33, 34].

$$ND_{\mathrm{max}} = \frac{N_{\mathrm{b}}}{2} \qquad \text{when } N_b \text{ is even} \tag{2.33}$$

$$ND_{\mathrm{max}} = \frac{N_{\mathrm{b}} - 1}{2} \qquad \text{when } N_b \text{ is odd} \tag{2.34}$$

In a forced response analysis of an impeller, the rotation of the blades leads to a travelling wave as long as the system features identical blades without mistuning. The individual blades experience the same force, but out of phase with the neighboring blades. The inter-blade phase difference, ϕ_{IBPD}, depends on the number of blades, N_{b}, and the engine order, EO, and is expressed by equation 2.35 for the ith blade of the rotor [35, 33]. The engine order is defined as the number of disturbances per rotation of the impeller.

$$\phi_{\mathrm{IBPD}} = \frac{2\pi \cdot EO \cdot (i-1)}{N_{\mathrm{b}}} \tag{2.35}$$

According to Singh et al. [34], the engine order and the nodal diameter should be same for resonance. However, when the engine order is higher than the maximum number of nodal diameters, a mode shape with nodal diameters less than the engine order will be excited. The following relationship can be applied to find the number of nodal diameters, ND, for of an excited mode [33, 34].

$$ND = |EO - m \cdot N_{\mathrm{b}}| \tag{2.36}$$

Here, m is an integer greater than or equal to 0. The visual representation of equation 2.36 is known as a Zig-zag shaped excitation line in the nodal diameter versus frequency (ZZENF) diagram. Figure 2-8 shows a ZZENF diagram of an impeller with a maximum number of nodal diameters of 11, taken from [34]. The associated values of m are also shown. In this example, a mode shape with 5 nodal diameters can be excited by an engine order of 5, 18, 28, 41, 51, 64 and 74.

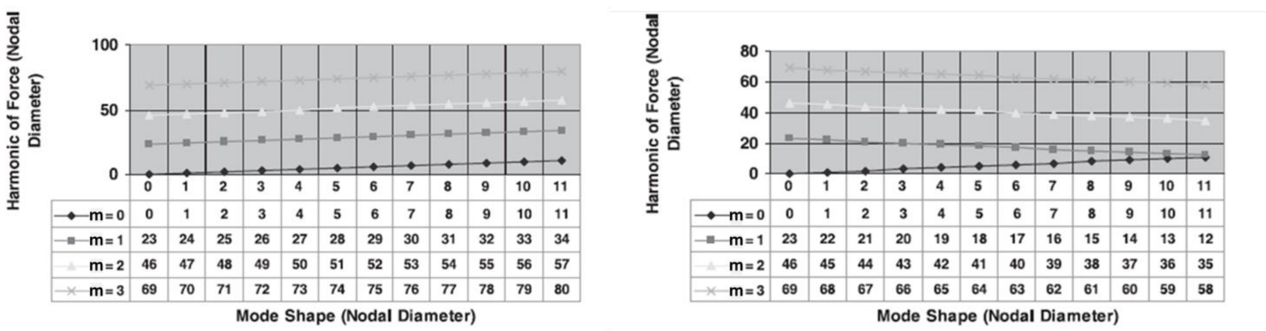

Figure 2-8: ZZENF diagram of an impeller with a maximum number of nodal diameters of 11 [34]

To get an idea of the regional vibration excitation in a system, a Campbell diagram can be drawn. A Campbell diagram consists of engine rotational speed in its x axis and system frequency in its y axis. The engine order lines are straight lines from the origin showing different engine order, e.g., one half engine order, two times engine order, ten times engine order etc. The Campbell diagram is a good way of understanding if a natural blade frequency is excited by a running frequency. The running frequency, f, of a compressor can be determined from its rotational speed, ω, or its revolutions per minute, RPM, and its engine order, EO, from equation 2.37.

$$f = \frac{\omega \times EO}{2\pi} = \frac{RPM \times EO}{60} \tag{2.37}$$

Figure 2-9 shows a typical Campbell diagram for a compressor rotating at a speed of 12000 rpm, and thus operating at a frequency of 200 Hz. If the first natural frequency of the compressor is calculated as 200 Hz, it will show an excitation while operating at 12000 rpm. After the calculation of the blade natural frequency, a natural frequency band has to be defined. For example, in Figure 2-9, a natural frequency band is defined between 190 Hz and 215 Hz. Thus, the compressor should be prohibited from operating at speeds between 11700 rpm and 12600 rpm [36]. Furthermore, the number of sources of excitation must be checked to determine the engine order of the compressor.

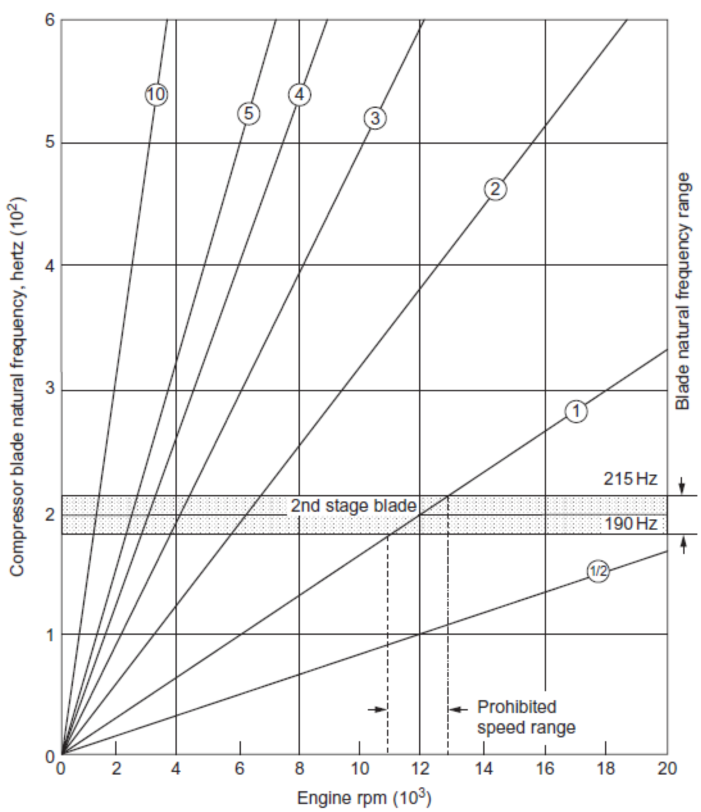

Figure 2-9: A typical Campbell diagram [36]

3 Model for Finite Element Analysis (FEA)

3.1 Overview

Finite element analysis (FEA) is a computational method to solve complex mathematical models to investigate certain properties, e.g., mechanical stress and strain, of a structure. It is a powerful tool in performing design analyses of parts or assemblies and is essential in solving models that are too complex to solve analytically. FEA solves these complex models by discretizing the entire domain (geometry) into subdomains known as elements. The process of discretizing is more commonly known as meshing. FEA eliminates the use of real objects in the early stages of a design process and thus saves costs associated with building and performing tests on a physical model [37].

In order to predict the durability and life cycle of the impeller that is being investigated in this thesis, a stress analysis was performed using FEA with Ansys Workbench. The main steps of the analysis include designing of the part with a Computer Aided Design (CAD) tool, defining the mechanical properties of the material used for the part, defining the contacts and connections between the different parts of the full model, generating a mesh with suitable element sizes, defining the loads and the boundary conditions, and finally analyzing the stress distribution and deformation results after solving. A model of the impeller, along with the shaft and other associated parts, was designed with the CAD software CATIA and further modified using Autodesk Inventor. The chosen material for the impeller is annealed Ti-6Al-4V. A detailed description of the complete model is given in the following sections (section 3.2 to 4.2).

3.2 Design of the model

As mentioned in the previous section, the geometry of the model was created using CATIA and further tweaked using Autodesk Inventor. Figure 3-1 shows the complete design of the assembly. The impeller is coupled to the shaft by pressing two springs against the impeller with a lug nut that is connected to the front end of the shaft. A support on the back of the impeller (support 1 in Figure 3-1) aids in the impeller staying in place and not sliding along the length of the shaft. The springs are situated on the shaft and inside the bore of the impeller. There are two bearings attached to the shaft and a support (support 2 in Figure 3-1) between the bearings. The length of the shaft is 104.6 mm.

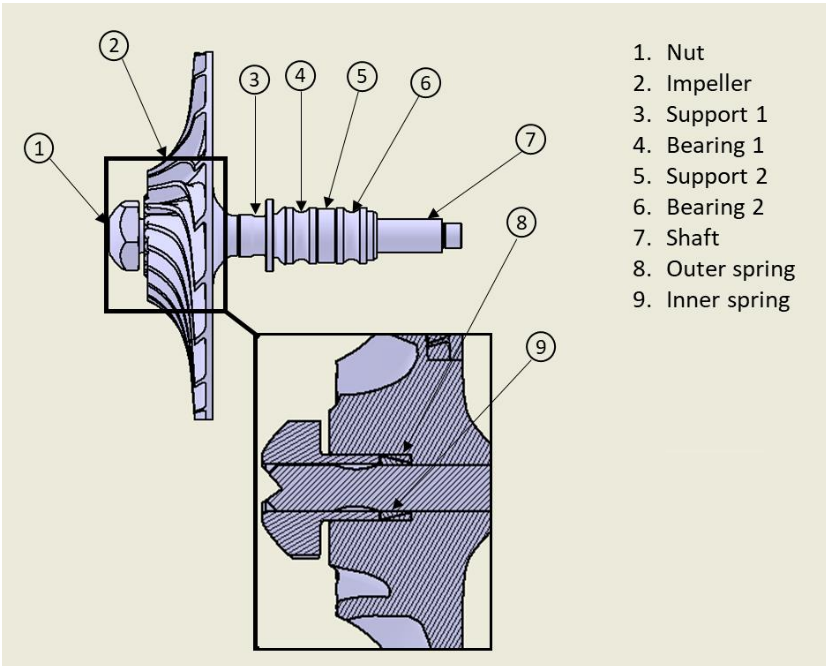

Figure 3-1: Geometry of the model including all of the parts

Figure 3-2 shows the isometric, front and side views of the impeller. The diameter of the impeller is 110 mm with a shaft opening of 11 mm. The disk has a thickness of 1.95 mm on the outer edge.

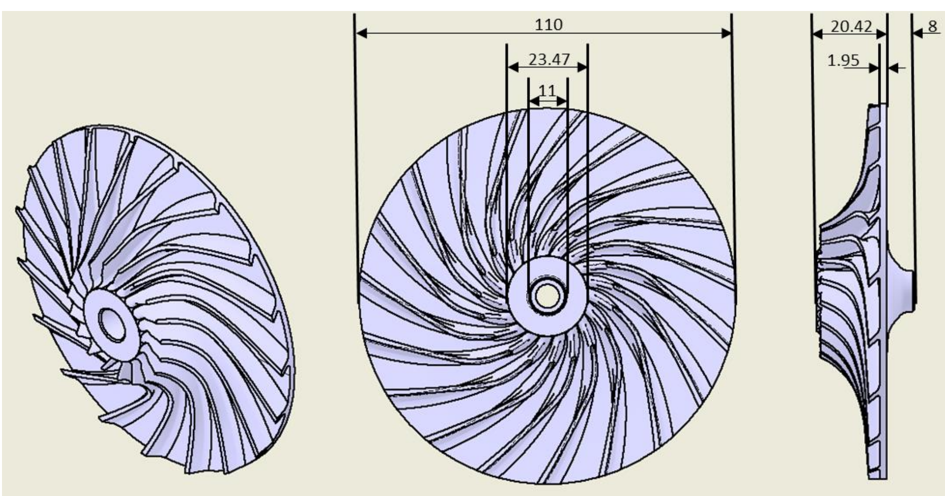

Figure 3-2: Geometry of the impeller with dimensions in mm showing the isometric view, front view and side view respectively

To reduce the computational time and to achieve a homogeneous mesh, the whole model was also simulated by applying a cyclic symmetry to a sector of the whole model while keeping the loads and the boundary conditions the same as the full model. The stress results of the models were then compared to analyze any difference in result between the models. For this, one nineteenth of the whole geometry was cut from the original CAD geometry using a cutting profile, as shown in Figure 3-3. The left diagram in Figure 3-3 shows the complete geometry with the cutting profile placed on it. The right diagram in Figure 3-3 shows the geometry after being cut.

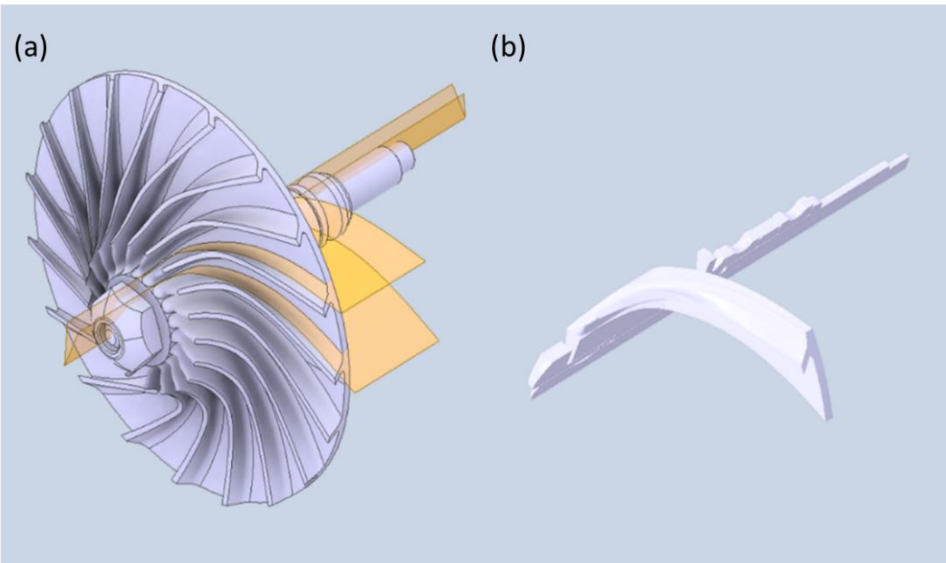

Figure 3-3: (a) full model of the impeller (b) a section of the model (one nineteenth of the whole model)

Furthermore, the compressor has a diffusor with 14 blades. Figure 3-4 shows the compressor assembly with the diffusor and its 14 blades as well as a cross-section of the full assembly. The static-mechanic simulation only includes the impeller and excludes the diffusor. The figure is only shown for illustrative purposes. Figure 3-5 shows the real-life construction of the full compressor assembly with the impeller inside and the diffusor outside.

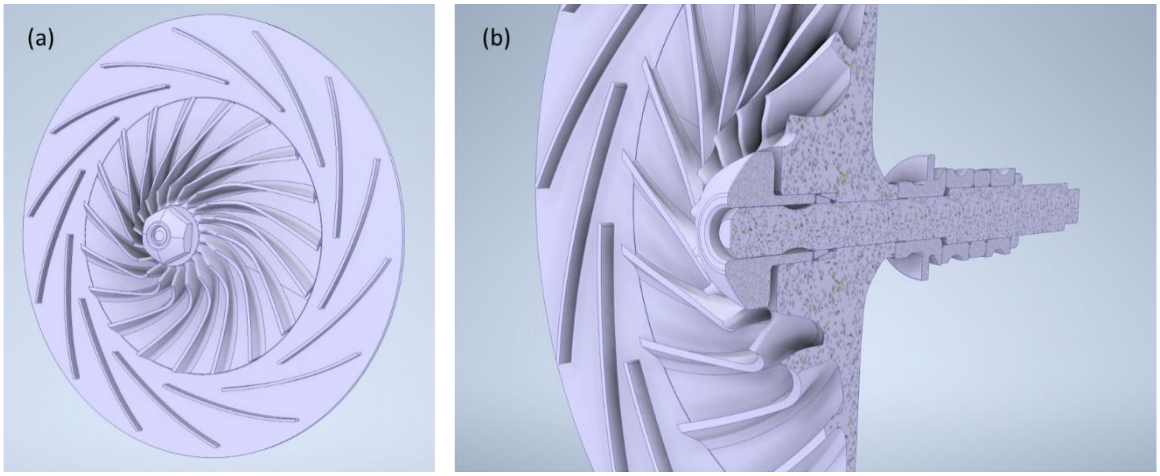

Figure 3-4: (a) Compressor assembly with the diffusor (b) Cross-section of the compressor assembly

Figure 3-5: Real-life construction of the compressor assembly

3.3 Selection of material

Titanium alloy is one of the more commonly used materials for compressors. Titanium alloys have a number of significant advantages over other alloys, e.g., steel, aluminum and nickel. Compared to steel alloys, titanium alloys have higher strength to weight ratio. Furthermore, compared to steel and aluminum alloys, titanium alloys can operate at a very high temperature (up to 600° C), and have high corrosion resistance due to its ability to make a natural oxide film that prevents it from oxidation [38, 39]. Additionally, titanium alloys also have high fracture toughness. The most commonly used titanium alloy is Ti-6Al-4V, accounting for almost half of the total titanium alloy market share, due to its characteristics of being lightweight and having high strength. Ti-6Al-4V has a maximum operating temperature of 315° C and is used in jet engines and rotating components, e.g., compressors in gas turbines [40, 41]. Above this temperature, the yield strength of the alloy decreases significantly, as can be seen in Table 3-1 [42].

Table 3-1: Dependence of temperature on the yield strength and Young's modulus of Ti-6Al-4V [42]

Temperature (° C)	Young's modulus (GPa)	Yield strength (MPa)
23	125	1000
260	110	630
316	100	630
427	100	525
482	80	500
538	74	446
650	55	300
800	27	45
825	20	25
850	5	5

The physical and mechanical properties of Ti-6Al-4V at standard temperature are presented in Table 3-2. The values are obtained from the manufacturer of the compressor used in this thesis. The definitions of these properties are discussed in detail in sections 2.1, 2.3 and 2.4.2.

Table 3-2: Physical and mechanical properties of annealed Ti-6Al-4V alloy (grade 5)

Property	Value	Unit
Density, ρ	4.43	g/cm^3
Brinell hardness, HB	334	-
Modulus of elasticity, E	113.8	GPa
Yield strength, σ_y	880	MPa
Ultimate tensile strength, σ_u	950	MPa
Elongation at break, eL	14	%
Poisson's ratio, ν	0.342	-

Fatigue properties of the material, i.e., fatigue strength coefficient, σ_f', fatigue ductility coefficient, ε_f', cyclic strain hardening exponent, n, and cyclic strength coefficient, H, can be calculated from these mechanical properties using equations 2.22, 2.23, 2.26 and 2.27

respectively. The calculated values of the fatigue properties are presented in Table 3-3. As mentioned in section 2.4.3, the values of fatigue strength exponent, b, and fatigue ductility exponent, c are taken from [27]. It has to be noted that, in the simulation, the value of n was taken as 0.0345 instead of the calculated 0.018, as an n value lower than 0.03 in Ansys Workbench produces a solver error [43].

Table 3-3: Fatigue properties of annealed Ti-6Al-4V alloy (grade 5)

Property	Value	Unit
Fatigue strength coefficient, σ_{f}'	1644.5	MPa
Fatigue strength exponent, b	-0.09	-
Fatigue ductility coefficient, $\varepsilon_{\mathrm{f}}'$	0.25	MPa
Fatigue ductility exponent, c	-0.56	-
Cyclic strength coefficient, H	984.25	MPa
Cyclic strain hardening exponent, n	0.018	-

Due to the properties mentioned above, the material of the impeller for the stress simulation in Ansys Workbench is assigned as Ti-6l-4V.

The material chosen for the shaft is a low carbon steel alloy, namely, 18CrNiMo7-6. This material is extensively used in manufacturing high strained parts, e.g. shafts and gears, due to its toughness and high tensile strength [44]. The physical and mechanical properties of 18CrNiMo7-6 are given in Table 3-4.

Table 3-4: Physical and mechanical properties of 18CrNiMo7-6

Property	Value	Unit
Density, ρ	7.85	g/cm^3
Modulus of elasticity, E	210	GPa
Yield strength, σ_{y}	335	MPa
Ultimate tensile strength, σ_u	1200	MPa
Poisson's ratio, ν	0.3	-

The material used for the bearings is 52100 type steel, also known as 100Cr6, which is an ISO and European EN standard bearing steel. The majority of the bearings is made from this material due to its high hardenability [45]. The material for the outer and inner springs is X10CrNi18-8, an ultra-high strength spring steel with tensile strength as high as 1800 MPa [46].

All the materials used for the different components of the model are summarized in Table 3-5. The materials and their associated properties were individually defined in the Engineering Data of Ansys Workbench and assigned to each corresponding material as per the specifications obtained from the manufacturer of the compressor. The properties of all the materials can be found in Appendix A and their S-N curves in Appendix B.

Table 3-5: Materials for the different components of the model

Component	Material
Impeller	Ti-6l-4V
Shaft	18CrNiMo7-6
Lug nut	2007 Aluminum
Support 1	100Cr6
Bearing	100Cr6
Support 2	9SMnPb28K
Springs	X10CrNi18-8

3.4 Contacts and connections

It is important to define the contacts in an assembly in order to describe how the parts move relative to each other. There are five different types of contacts that can be defined in Ansys Workbench. The first type is called a Bonded contact, which replicates a contact region between two parts that are glued together without any separation or sliding. No Separation type of contact allows frictionless sliding between the parts without separation. The third type is known as Frictionless contact, where sliding between the parts is frictionless, but it is possible for the parts to separate from each other. Rough contact type assumes an infinite friction coefficient in the contact region, thus, sliding between the parts is not possible. The final type of contact is called Frictional contact, where the parts can move in relation to each other with a defined friction coefficient [47].

As described in section 3.2, there are nine different parts of the complete assembly of the model. It is essential to define proper contacts between the parts to simulate how the parts move relative to each other. Figure 3-6 shows all the contact regions of the model and their types. To simulate the lug nut being tightly screwed to the shaft without any relative movement between them, the contact between these two parts was defined as bonded. Furthermore, the shaft is also connected to the bearings by means of bonded contacts to prevent any sliding between them. The contact between the shaft and the impeller, as well as the contacts between the shaft and the supports, was defined as frictionless. This was done to simulate a small gap for tolerance between these parts. All the other contacts were defined as frictional with specific frictional coefficients to allow relative sliding between the associated parts.

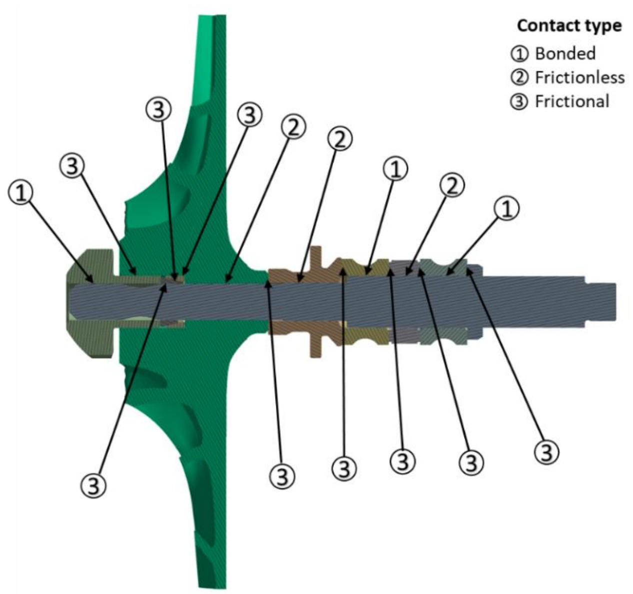

Figure 3-6: Contact types in different contact regions. 1-Bonded, 2-Frictionless, 3-Frictional

A summary of all the contacts and their types is given in Table 3-6. In case of frictional contacts, the associated frictional coefficients are also mentioned.

Table 3-6: Contacts and their types in the model

Contact	Target	Contact type	Friction coefficient
Lug nut	Shaft	Bonded	-
Shaft	Bearings	Bonded	-
Shaft	Impeller	Frictionless	-
Shaft	Supports	Frictionless	-
Inner spring	Lug nut	Frictional	0.30
Shaft	Inner spring	Frictional	0.30
Inner spring	Outer spring	Frictional	0.30
Impeller	Outer spring	Frictional	0.30
Impeller	Support 1	Frictional	0.30
Bearing	Support 1	Frictional	0.30
Support 2	Bearing	Frictional	0.30

Two joints were defined in the two bearing regions using the stiffness coefficients of a deep groove ball bearing. The stiffness values of the two bearings were obtained from the data sheet provided by the supplier and are given in Table 3-2.

Table 3-7: Stiffness values of the bearings used in the model

Longitudinal stiffness (N/mm)			Rotational stiffness (N/rad)		
x	y	z	x	y	z
23000	56000	56000	0	6.8755e7	6.8755e7

3.5 Meshing

Meshing in FEA is the process of discretizing the whole domain into a finite number of small subdomains. These subdomains are known as elements. Each element has a number of nodes by which the element is connected to the adjacent elements. Figure 3-7 shows the types of elements that can be used for performing a 3D analysis. A quadratic element has more nodes than a linear element permitting more degrees of freedom, and in turn, allowing a more accurate result in a stress analysis [47, 48].

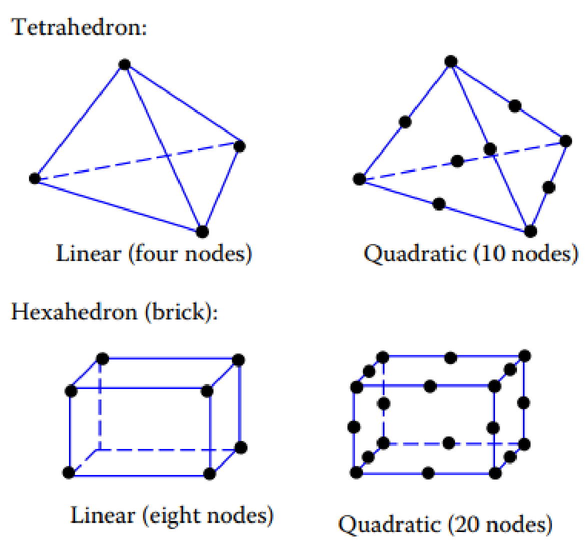

Figure 3-7: Types of FEA elements [47]

The model was solved using mostly hexahedron type elements. In places where hexahedron type elements were not possible, tetrahedron type elements were used. In both cases, quadratic elements were used by setting the Physics Preference to non-linear. A mesh study was done in the model to obtain optimum element sizes for the different components. This was done by solving the model with a course mesh, i.e., larger element size, at the beginning. The model was then solved repeatedly by making the element size smaller until the result of the averaged and unaveraged stress analysis yielded similar result. The mesh study method is given in Appendix C. Further considerations were made to match the size of the elements of two bodies sharing a contact. Element sizes of the different regions of the model are given in Table 3-8.

Table 3-8: Element sizes of the different areas

Component	Element size (m)
Global	0.00125
Impeller	0.001
Shaft opening of impeller	0.0005
Shaft	0.0005
Support 1	0.0005
Bearings	0.0004
Support 2	0.00025
Springs	0.00025

3.6 Loads and boundary conditions

3.6.1 Loads

In the simulation, four different loads were considered to be acting on the impeller. These are the load due to the rotational velocity of the impeller, load due to the applied thermal condition based on the operating temperature of the impeller but is taken as constant due to the absence of a Computational Fluid Dynamics (CFD) data of the temperature field, pressure on the front of the impeller obtained from the CFD data, and pressure on the back of the impeller. A further preload was defined as a bolt pretension due to the pressing of the lug nut on the springs.

The loads were applied in four simultaneous load steps to achieve better convergence and simulate different operating conditions. The bolt pretension was defined in the first load step. All the other loads were set to zero in this step. This implies that, in the first load step, the only load acting on the model is the preload from the nut. The preload was defined on an area of the shaft that does not have any contact regions on it with a value of 4370 N. This value was obtained from the torque specification provided by the supplier of the lug nut. Figure 3-8 shows the area of the shaft (marked in red) that is used to define the bolt pretension.

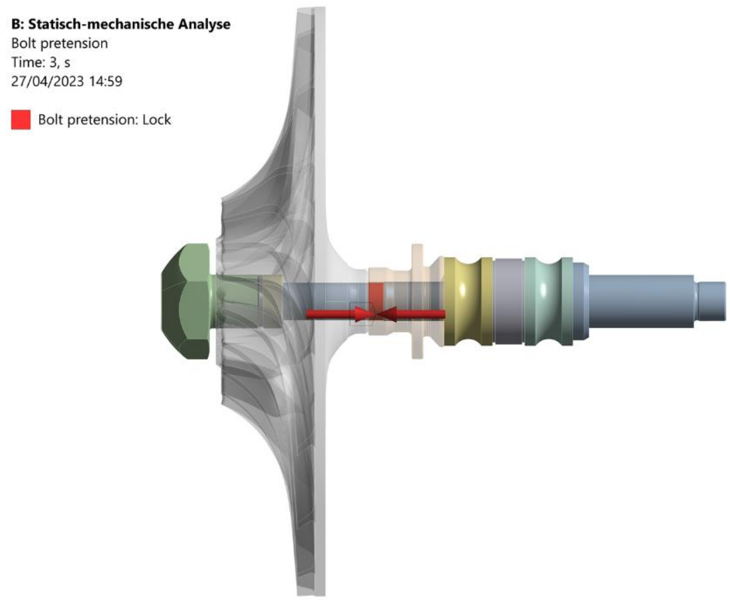

Figure 3-8: Bolt pretension, defined on an area of the shaft (marked in red) that does not have any contact regions

The impeller, along with the other parts, rotates at a maximum rotational speed of 11000 rad/s or about 105000 rpm. The speed was set to 7000 rad/s in the second load step and was increased to the maximum speed in the subsequent load steps. The rotational speed of all the components of the assembly was defined by specifying a coordinate system on the axis of the impeller and setting the axial component of the rotational speed for the whole assembly to the defined value.

The temperature of the whole assembly was set to 22° C in the first load step and increased to 280° C in the next two load steps. In the final load step, the temperature was set to the maximum value of 350° C. Due to the absence of CFD data, the same temperature is assumed for the whole impeller as well as the different parts of the assembly. However, in reality, the temperature of the impeller would be different in the different areas of the impeller, similar to Figure 3-9.

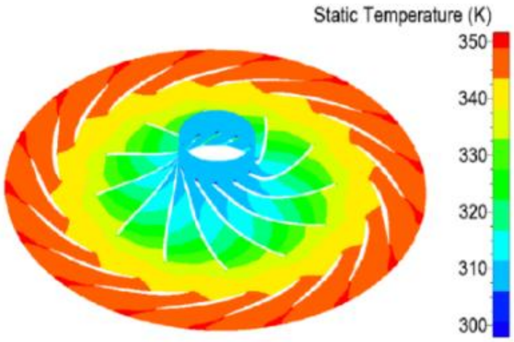

Figure 3-9: Temperature distribution of a compressor impeller [49]

The pressure on the front of the impeller was mapped using data obtained from a CFD calculation and was applied from the second load step. Figure 3-10 shows the mapped pressure field on the front of the impeller.

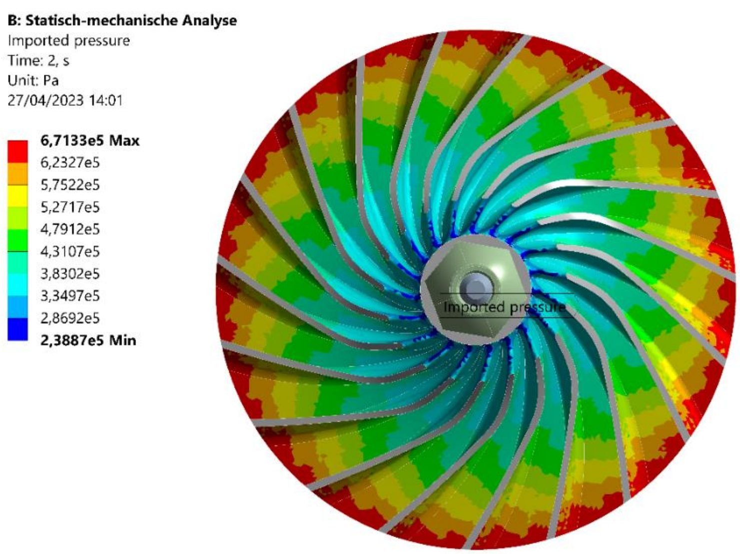

Figure 3-10: Pressure load on the front of the impeller obtained from CFD data (comma used instead of dot as decimal point due to the language of Ansys set to German)

Based on experience, the pressure on the back of the impeller was assumed to be about 80% of the maximum pressure on the front and was set to 0.5 MPa. The pressure was applied normal to the back surface of the impeller (Figure 3-11) from the second load step.

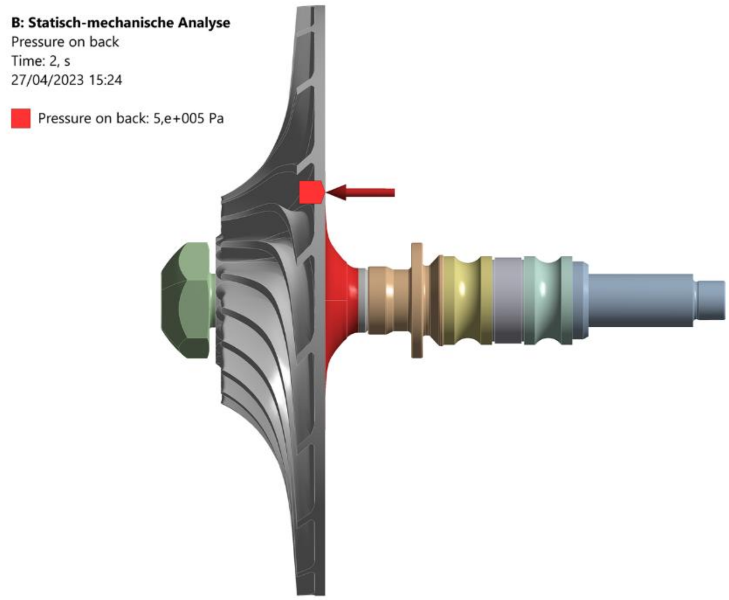

Figure 3-11: Applied pressure, normal to the back of the impeller (comma used instead of dot as decimal point due to the language of Ansys set to German)

All the loads applied to the model are summarized in Table 3-9.

Table 3-9: Loads applied to the model

Load	Load step 1	Load step 2	Load step 3	Load step 4
Preload in bolt pretension (N)	4370	0	0	0
Rotational velocity (rad/s)	0	7000	11000	11000
Temperature (° C)	22	280	280	350
Pressure on impeller front (Pa)	0	CFD data	CFD data	CFD data
Pressure on impeller back (Pa)	0	5E5	5E5	5E5

3.6.2 Boundary conditions

In order to prevent rigid body motion, a Displacement boundary condition with a polar coordinate system was defined by setting the rotational component of the Displacement to fixed, and the axial and the radial component to free. The axial and radial movements of the assembly were fixed by the two bearing regions.

3.7 Modal analysis

In order to find the natural frequencies and the associated mode shapes of the impeller, a modal analysis was performed only on the impeller. A static-mechanic analysis was done prior to the modal analysis. However, since only the impeller was used, a remote displacement boundary condition, with displacements along all axes and rotation with respect to all axes set to zero, was used on the surface where the shaft would otherwise be connected to the impeller. The maximum frequency of the modal analysis was set to 1.5 times the frequency of the harmonic response analysis, since Ansys WB requests natural frequencies 1.5 times higher than the highest forcing frequency. The preload, rotational speed, thermal condition and pressures remained the same as given in Table 3-9. The solution of the static-mechanic analysis was used as a pre-stress condition to the modal analysis.

3.8 Harmonic response analysis

The harmonic response analysis was done by applying a modal superposition method. Due to the absence of transient CFD pressure data, an imaginary force of 1 N was applied tangentially to each of the blades. The magnitude of the force was then increased until the stress reached the yield strength of the material. The engine order was determined to be 14 due to the compressor having 14 diffusor blades. The inter-blade phase angle for each of the blade is calculated using equation 2.35. The difference in phase angle between two adjacent forces is 265.26°. Figure 3-12 shows the applied forces for the harmonic response analysis. From equation 2.37, the operating frequency of the impeller rotating at its full speed of 105000 rpm is determined to be 24500 Hz. Thus, the harmonic response analysis was done for a frequency range of 22500 Hz to 26500 Hz. The response was observed at a node on the tip of a randomly selected blade (shown by the black dot in Figure 3-12).

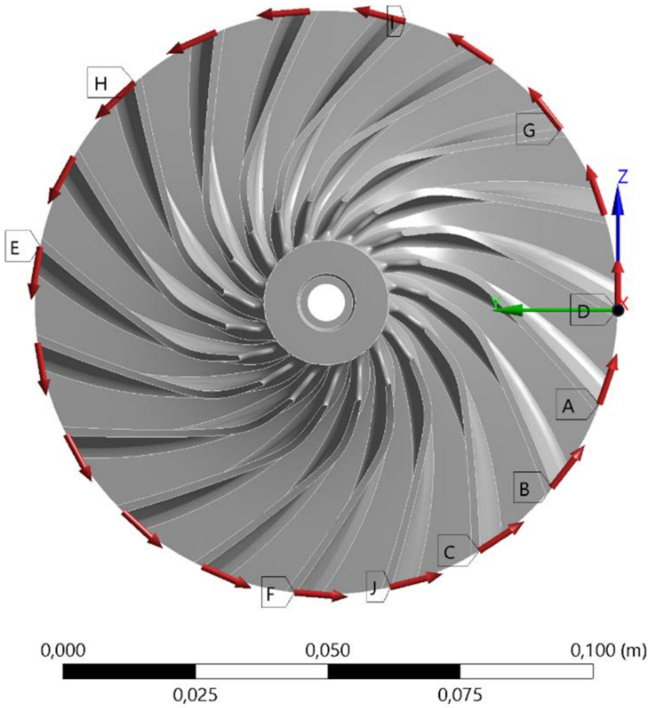

Figure 3-12: Forces applied tangential to the blades for the harmonic response analysis with the response observed at a point (marked with a black dot) on the tip of a randomly selected blade

To plot the Campbell diagram, the modal analysis was done for 0%. 25%, 50%, 75% and 100% of the maximum rotational speed of the impeller. The frequencies of the excited mode shape are then plotted against their associated rotational speeds to see if the curve intersects with the engine order line.

4 Results and discussion

4.1 Stress and strain analysis

The stress analysis of the impeller is done based on the maximum distortion energy theory, also known as the von Mises stress theory (see section 2.2). The von Mises stress is a measure of all the normal and sheer stresses acting on the body. This gives an estimation of the combined stress acting on an area and is helpful in locating regions with high stresses.

Figure 4-1 (a) shows the front view of the impeller, where it can be seen that the stress in areas where the blades meet the disk is higher compared to the adjacent regions of the disk. The rotation of the impeller causes a bending stress on the connection of the blades and the disk due to the moment of the blades, creating these high-stress regions. This stress is also observed in the studies by Nandi and Ghosh [50] and Kienzle et al. [51]. The high stress region of the disk due to the blades is also observed on the back of the impeller, shown in Figure 4-1 (b). The highest stress on the front of the impeller is observed close to halfway along the length of the blades. The axial load on the impeller due to the pressure field causes a bending stress in this region of the disk. The axial stress on the impeller disk, along with the tensile stress due to the blades, causes a high stress region halfway between the inner and the outer edge of the impeller.

The high-stress region on the back of the impeller, shown in Figure 4-1 (b), is a result of the circumferential stress, also known as tangential stress or hoop stress, and the radial stress. Several studies can be found that describe the circumferential stress and the radial stress in a rotating annular disk with varying thickness similar to an impeller of a compressor. Allam et al. [52] performed an analytical stress analysis on a rotating functionally graded annular disk and a solid disk with gradually varying thickness. The geometry of the annular disk presented in this study closely mimics a compressor disk. They found out that the radial stress in the annular disk is maximum at a radius that is about 40% of the radial distance between the inner and the outer edge of the disk. The circumferential stress is maximum at the inner edge and decreases with the increase in radial distance. A similar result is also shown in a study of stress function of a rotating variable-thickness annular disk by Zenkour et al. [53], where the radial stress is maximum at a radius similar to [52], while the circumferential stress is maximum at the inner edge of the disk.

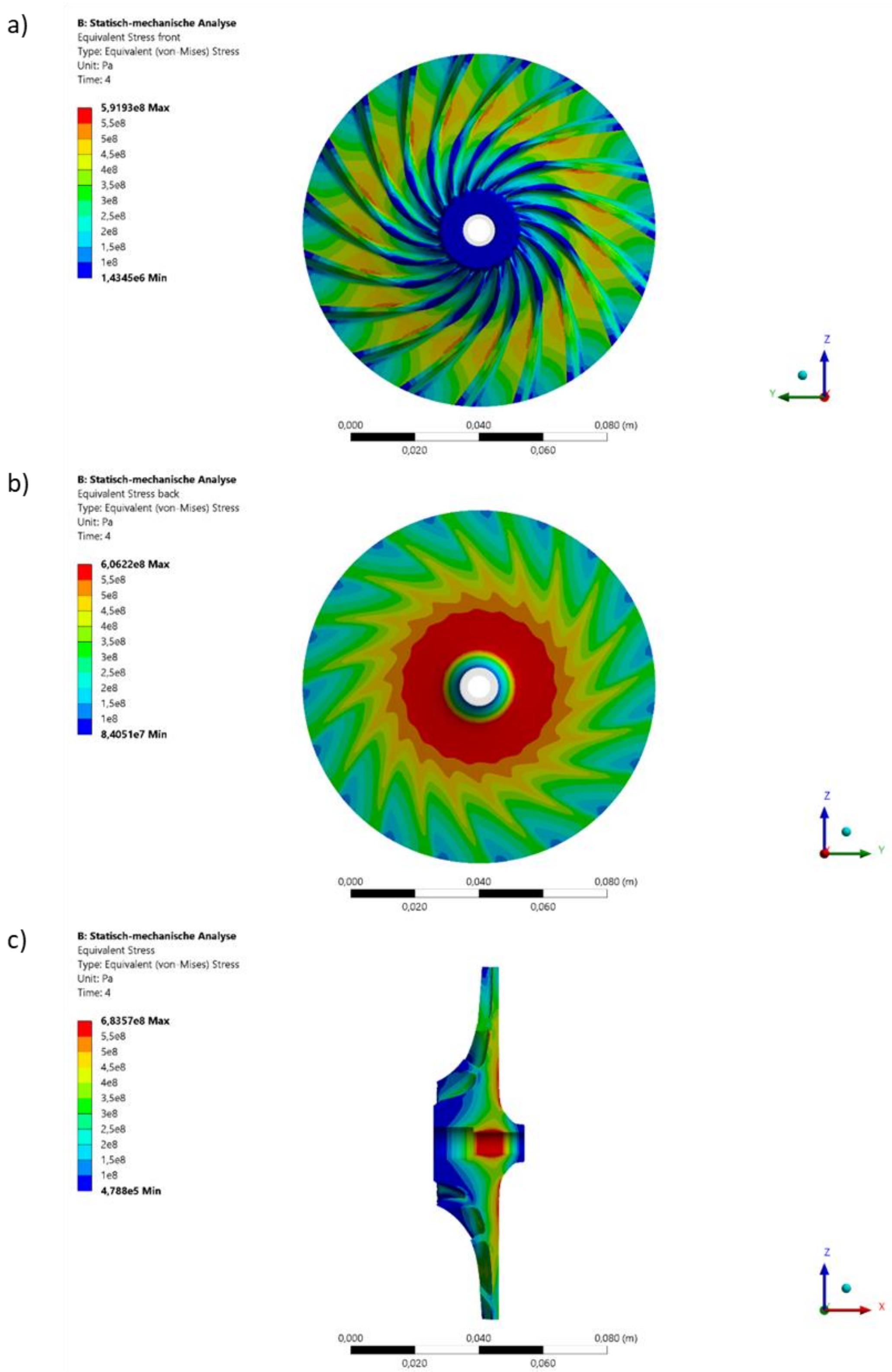

Figure 4-1: Stress distribution of the impeller’s (a) front view, (b) back view and (c) section view

When the circumferential stress and the radial stress are taken as the two principal stresses in the von Mises criterion, it is seen that the von Mises stress is maximum at the inner edge of the disk and decreases with the increase in radius. This phenomenon can be seen in Figure 4-1 (b).

The high stress in the bore region, seen in Figure 4-1 (c), is caused by the circumferential stress due to the centrifugal force of the rotating impeller. The centrifugal force causes the bore region to expand when it is interference fit onto the shaft [54]. Łagodziński et al. [55] did a failure analysis of a centrifugal compressor impeller and saw that the high circumferential stress in the bore of the impeller was the cause of the failure of the impeller with the stress being even higher when the bore was interference fit onto the shaft.

A closer inspection reveals that the stress distribution throughout the impeller is not homogenous. This can be observed more clearly from Figure 4-2, where the two red areas, depicting the two high stress regions, do not have the same shape. The primary reason behind this can be attributed to the inhomogeneous distribution of elements in these areas as a result of the meshing done for the entire geometry without applying any cyclic symmetry.

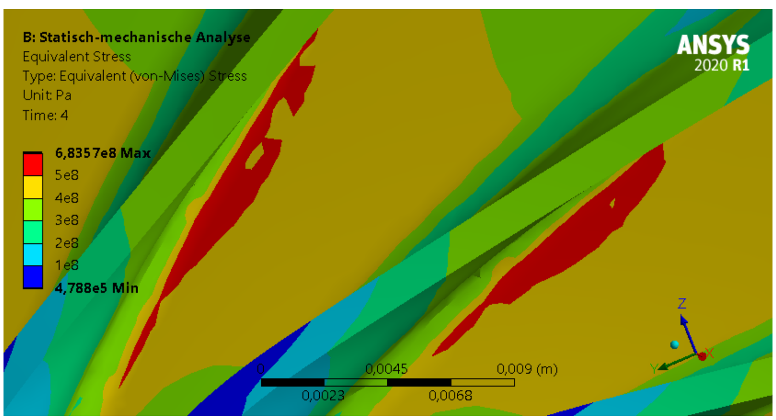

Figure 4-2: Inhomogeneous stress distribution on the disk in the areas near the blades due to inhomogeneous meshing

In order to address the issue of this inhomogeneous mesh, the model was also solved by applying a cyclic symmetry to a section of the impeller. Since the impeller has 19 blades and the section model is 1/19th of the whole model (see section 3.2 for the complete description of the full and the section geometry), the analysis is done only on one blade. The use of cyclic symmetry ensures that the stress result is the same in all the 19 sections.

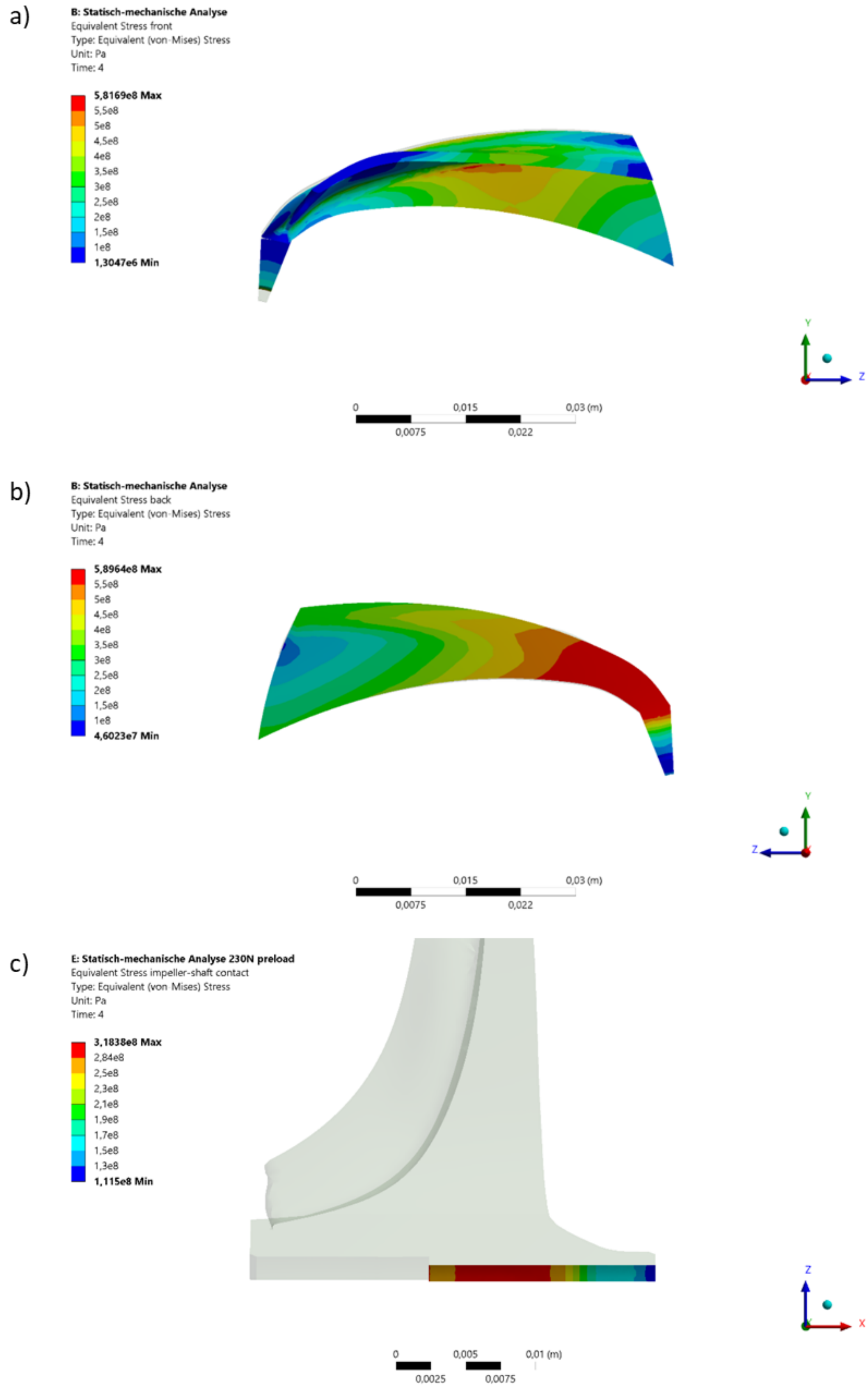

Figure 4-3: Stress distribution of the impeller's (a) front view, (b) back view and (c) bore region in the sector model

As can be seen in Figure 4-3, the stress distribution of the sector shows that the high-stress regions are similar to the full model. The maximum stress values at the front and the back of the impeller are also close. However, there is a significant difference between the two models regarding the maximum stress at the bore region of the impeller. The sector model shows a much lower maximum stress at the bore region. The most plausible reason behind this is that while the sector model correctly shows the circumferential stress at this area, it omits the stress due to the interference fit of the impeller onto the shaft. Figure 4-4 shows the maximum stress values after every time step. As can be seen in Figure 4-4 (c), the maximum stress value at the bore region is much lower than the full model after each time step. This further shows that a portion of the stress is being omitted in the stress analysis of the bore region of the sector model.

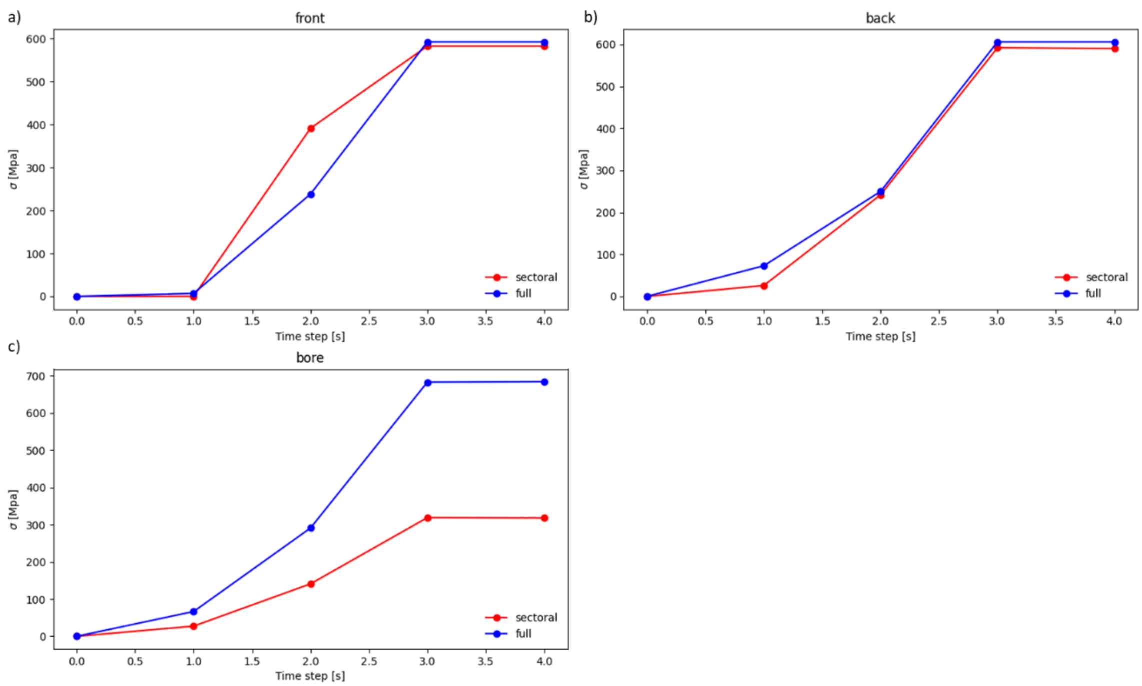

Figure 4-4: Maximum stress values of the full and sector models at the impeller's a) front, b) back and c) bore region after each time step

Figure 4-4 also shows that the stress as a result of the preload due to the bolt pretension is much lower in the sector model, since the stress after the first time step, where only the preload is applied, is always much lower compared to the full model. The preload in Ansys WB only works with cylindrical or circular objects. As such, it is not possible to correctly define a preload in a cyclic symmetry model, since such a model only works with a sector of the full object. Due to these limitations, the stress analysis of the full model is used to calculate the fatigue life of the impeller.

The maximum stresses in the three critical areas of the impeller for the full model, along with what percentage they are of the yield stress of Ti-6Al-4V, are listed in Table 4-1. The values are well below the manufacturer's specified yield stress of the impeller material, namely Ti-6Al-4V. However, since the model is simulated with a thermal condition of 350 °C, the maximum stresses of the impeller are very close or, in the case of the bore region, exceeds the yield stress of Ti-6Al-4V at 350 °C. It also should be noted that the temperature of the impeller at the bore region should be lower than the constant specified temperature of 350 °C. Due to the absence of a temperature field from CFD calculation, this could not be correctly applied in the model.

Table 4-1: Maximum stresses in the critical regions of the impeller

Region	Maximum stress (MPa)	% of yield stress (manufacturer's specification)	% of yield stress at 350 °C
Front	590	67 %	94 %
Back	605	67 %	96 %
Bore	684	77 %	108 %

In order to analyze the stress during a complete rotation of the impeller, 19 different points with the same radial distance from the center of the impeller were defined with equal angular distance between them. This simulates one point on the impeller doing a complete rotation. This is a good way to understand the stress and strain that the point goes through at different angular displacements. In order to perform this, a separate coordinate system was defined for each point in Ansys. To find the positions of the points, a local coordinate system was defined at the center of the impeller. Then, a point of interest, e.g., a point in a high stress region, was defined in the global coordinate system. Afterwards, the coordinate of the point was transformed into the local coordinate system. Subsequently, a geometric calculation was done using equations 4.1 through 4.7 to calculate the coordinates of rest of the points in the global coordinate system.

$$y_1 = y_{1,\mathrm{glob}} - y_{\mathrm{loc}} \qquad z_1 = z_{1,\mathrm{glob}} - z_{\mathrm{loc}} \tag{4.1}$$

$$r = \ y_1{}^2 + z_1{}^2 \tag{4.2}$$

$$\alpha = \tan^{-1}\left(\frac{y_1}{z_1}\right) \tag{4.3}$$

$$\Delta\theta = \frac{360}{19} \tag{4.4}$$

$$\alpha_{\mathrm{n}} = 180° + \alpha + \alpha_{\mathrm{n}-1} + \Delta\theta \qquad for\ \alpha_{\mathrm{n}} < 360° \tag{4.5}$$

$$\alpha_{\mathrm{n}} = 180° + \alpha + \alpha_{\mathrm{n}-1} + \Delta\theta\ - 360° \qquad for\ \alpha_{\mathrm{n}} > 360°$$

$$y_{\mathrm{n}} = r\cos(\alpha_{\mathrm{n}}) \qquad z_n = r\sin(\alpha_{\mathrm{n}}) \tag{4.6}$$

$$y_{\mathrm{n}} = y_{\mathrm{n,glob}} + y_{\mathrm{loc}} \qquad z_{\mathrm{n}} = z_{\mathrm{n,glob}} + z_{\mathrm{loc}} \tag{4.7}$$

Here, y_1 and $y_{1,\mathrm{glob}}$ are the y coordinates of the first point of interest in the local and global coordinate systems respectively; y_n and $y_{\mathrm{n,glob}}$ are the y coordinates of the nth point of interest in the local and global coordinate systems respectively; y_{loc} is the y coordinate of the origin of the local coordinate system in the global coordinate system; z coordinates are named similar to the y coordinates; r is the radial distance between the point and the origin of the local coordinate system; α is the angle between the horizontal line through the origin of the local coordinate system and the line connecting the point and the same origin; α_{n} is the angle of the nth point; $\Delta\theta$ is the angular difference between the adjacent points. Figure 4-5 shows the defined points on the front and the back of the impeller. The x coordinates of all the points are the same for a face.

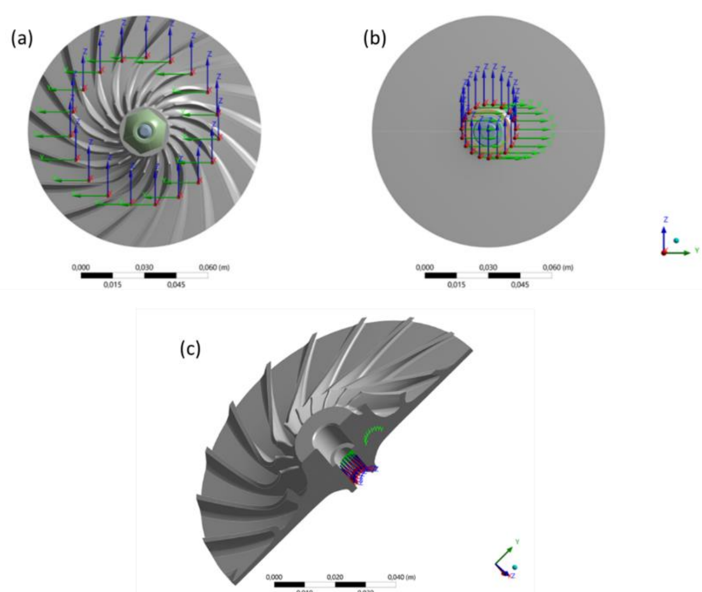

Figure 4-5: Defined points on the three critical regions, i.e., (a) the front of the impeller, (b) the back of the impeller, and (c) the bore of the impeller to analyze a complete rotation of the impeller

The stress values of these points on the three critical regions, i.e., the front, the back, and the bore of the impeller area are shown in Figure 4-6. The stress values range from about 490 MPa to about 535 MPa on the front, 535 MPa to about 545 MPa on the back, and 650 MPa to 660 MPa in the bore region of the impeller. As discussed before, this variation of stress is a result of the inhomogeneous distribution of elements. This problem can be addressed by either using a sector model with cyclic symmetry or making the mesh finer. As discussed before, the sector model could not be used due to its limitations. A finer mesh size would result in a higher computational time without having a significant effect on the fatigue life.

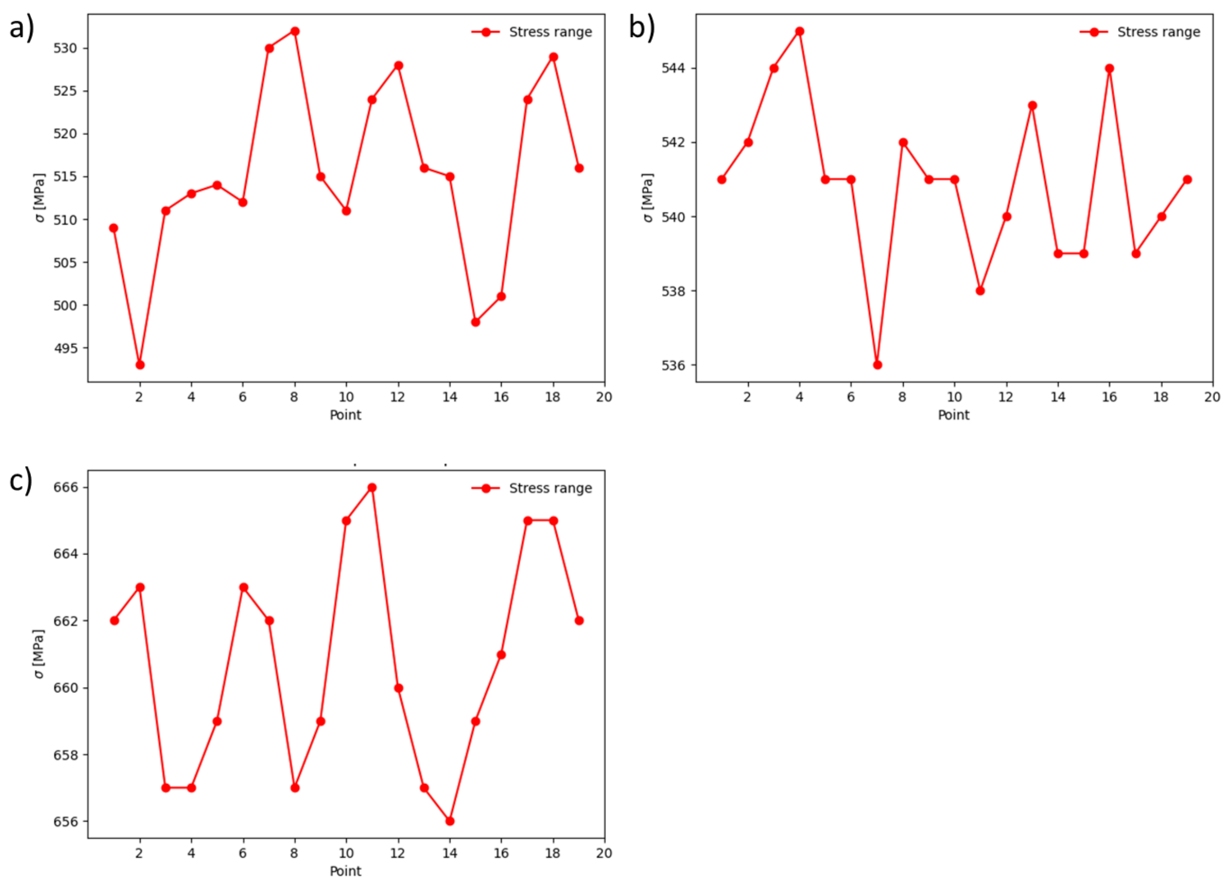

Figure 4-6: Stress values of the 19 defined points on (a) the front of the impeller, (b) the back of the impeller, and (c) the bore of the impeller

The total strain is calculated from the simulated stress values using the Ramberg-Osgood equation (equation 2.28). Furthermore, the elastic and plastic parts of the total strain are calculated using the elastic and plastic terms of the right-hand side of the same equation. Figure 4-7 shows the calculated elastic and plastic strain values of the defined points on the front, the back, and the bore area. It can be seen that the effect of plastic strain is almost negligible. This is expected as the stress values of these points are well below the yield point of the material of the impeller. Since the maximum stress values of the different critical areas of the impeller are similarly below the yield point of the material, it can be said that there is almost no plastic strain on the impeller. It should be noted that the yield stress of the material that was given as input to Ansys WB was taken from the manufacturer's specification rather than literature values at 350 °C. If the yield stress of the impeller material at 350 °C was taken from literature, the value would have been much lower. As a result, some plastic deformation could be expected.

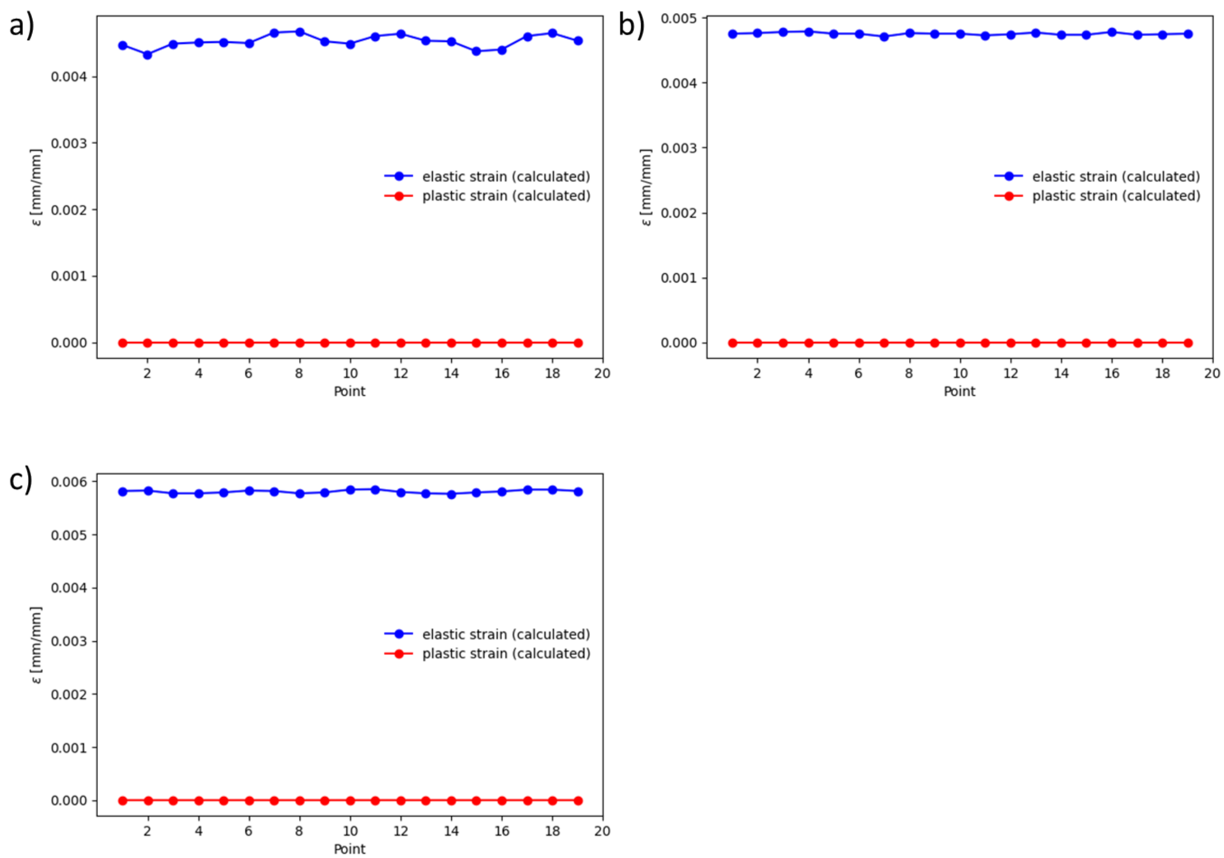

Figure 4-7: Elastic and plastic parts of the strain values of the 19 defined points on (a) the front of the impeller, (b) the back of the impeller, and (c) the bore of the impeller

Figure 4-8 shows a comparison between the calculated strain and the simulated strain. The small difference between the calculated and the simulated values is possibly due to numerical rounding error within the software. For the calculation of fatigue life in these points, the calculated strain values are used since they are obtained using the simulated stress values and is a more accurate representation of the total strain if the stresses are assumed correct. In any case, the difference is reasonably small compared to the total strain and does not have any significant effect on the fatigue life.

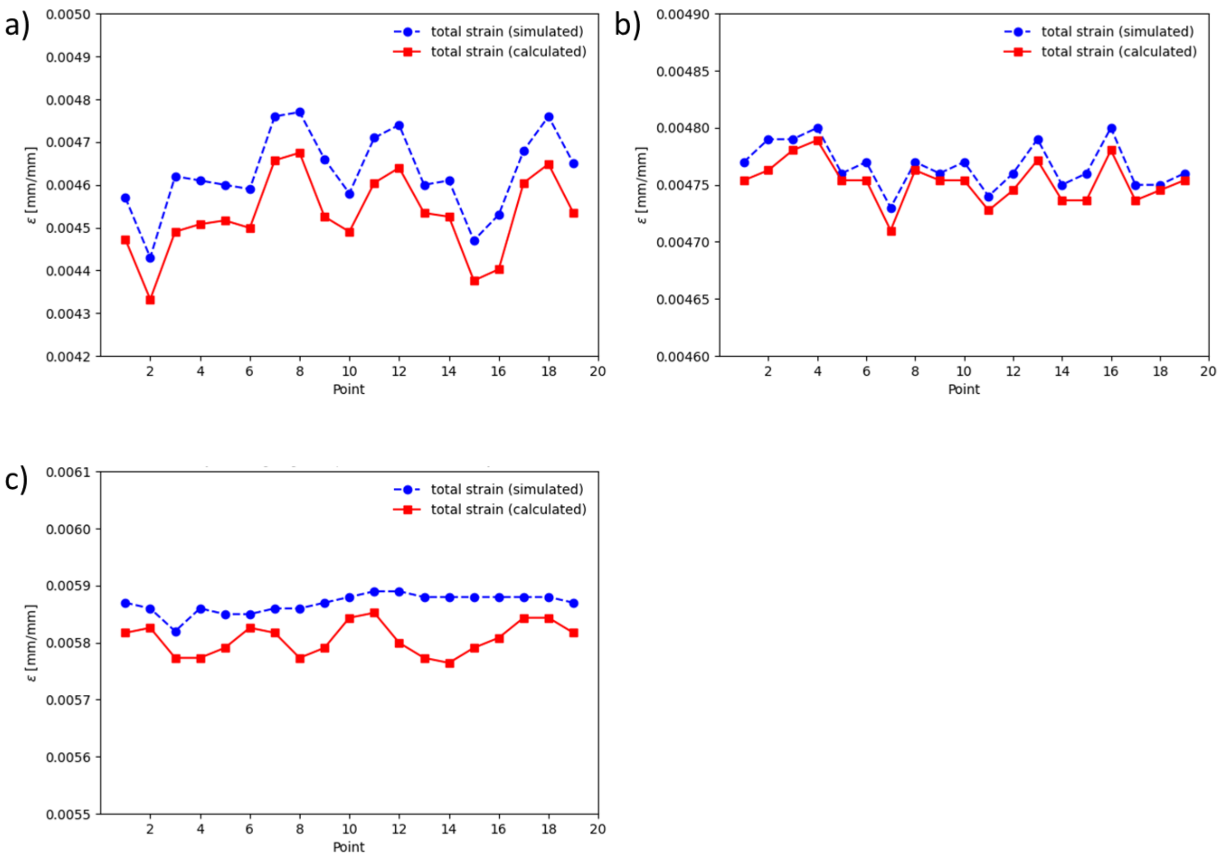

Figure 4-8: Comparison between calculated and simulated total strain of the 19 defined points on (a) the front of the impeller, (b) the back of the impeller, and (c) the bore of the impeller

4.2 Fatigue life analysis

The fatigue life of the impeller is calculated using the cyclic strain-controlled condition. As discussed in section 2.4.3, the number of cycles to failure, N_f, is calculated using the Manson-Coffin equation (equation 2.21). The parameters of the equation for the impeller material, namely, Ti-6Al-4V, are given in Table 3-3. Using the definition of stress amplitude from equation 2.13, the strain amplitude is first calculated by equation 2.28. The number of cycles to failure is then found by changing the variable N_f in equation 2.21 until the left-hand side of equation 2.21 becomes equal to the calculated strain amplitude. Since the analysis is done on a zero-based loading condition, one cycle means the load is taken to the maximum amplitude from zero and then taken back to zero. The stress ratio, in this case, is 0 (see equation 2.15). The results are then compared with the simulated fatigue life done in Ansys WB. Figure 4-9 shows the analytically calculated number of cycles to failure for the 19 defined points on the front, back and bore region of the impeller.

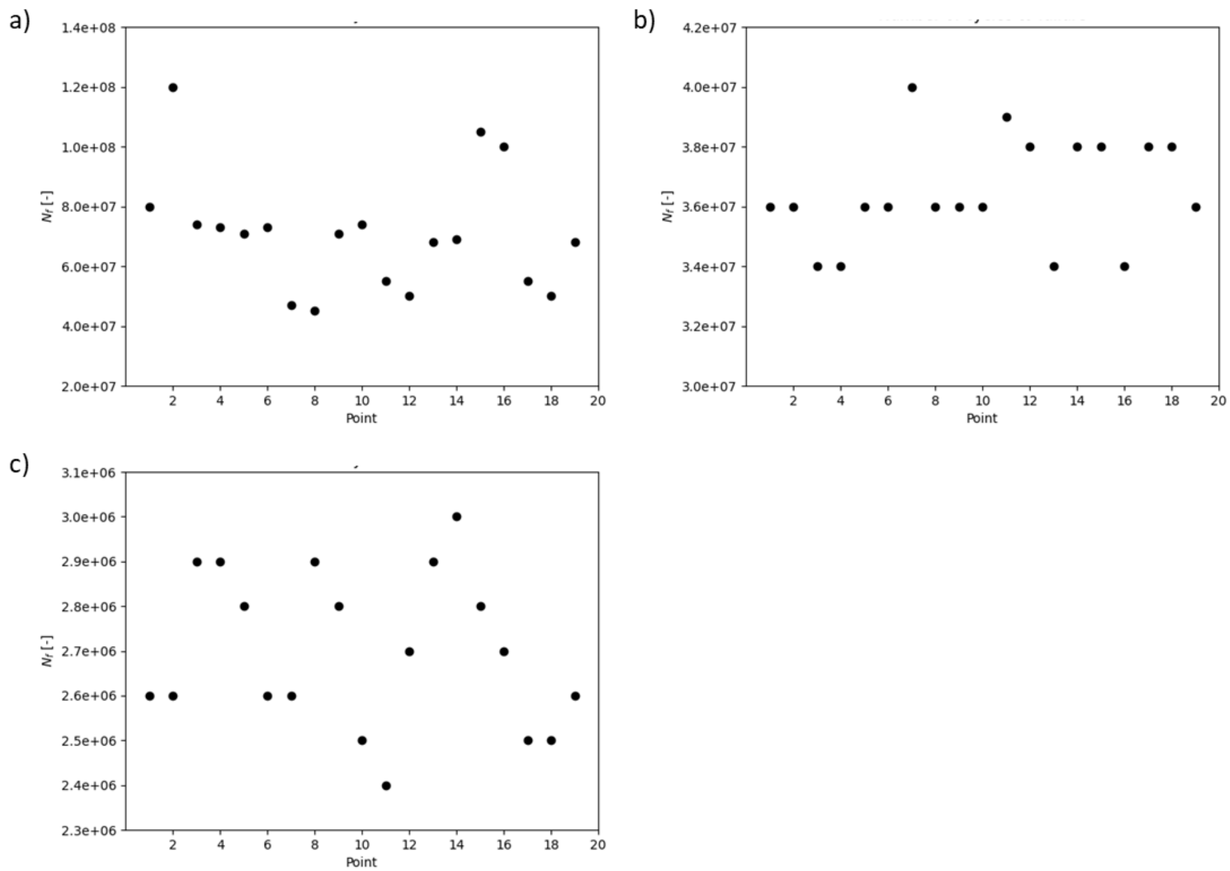

Figure 4-9: Calculated number of cycles to failure of the 19 defined points on the a) front, b) back and c) bore region of the impeller

Figure 4-10 shows the simulated result of the number of cycles to failure that was done using the fatigue tool of Ansys WB. On the front of the impeller, most of the points have a fatigue life below or equal to 7e7 cycles with four outliers. This fits well with the simulated result, where the critical regions (regions where the points are defined) on the front of the impeller show a fatigue life of below 7e7 cycles.

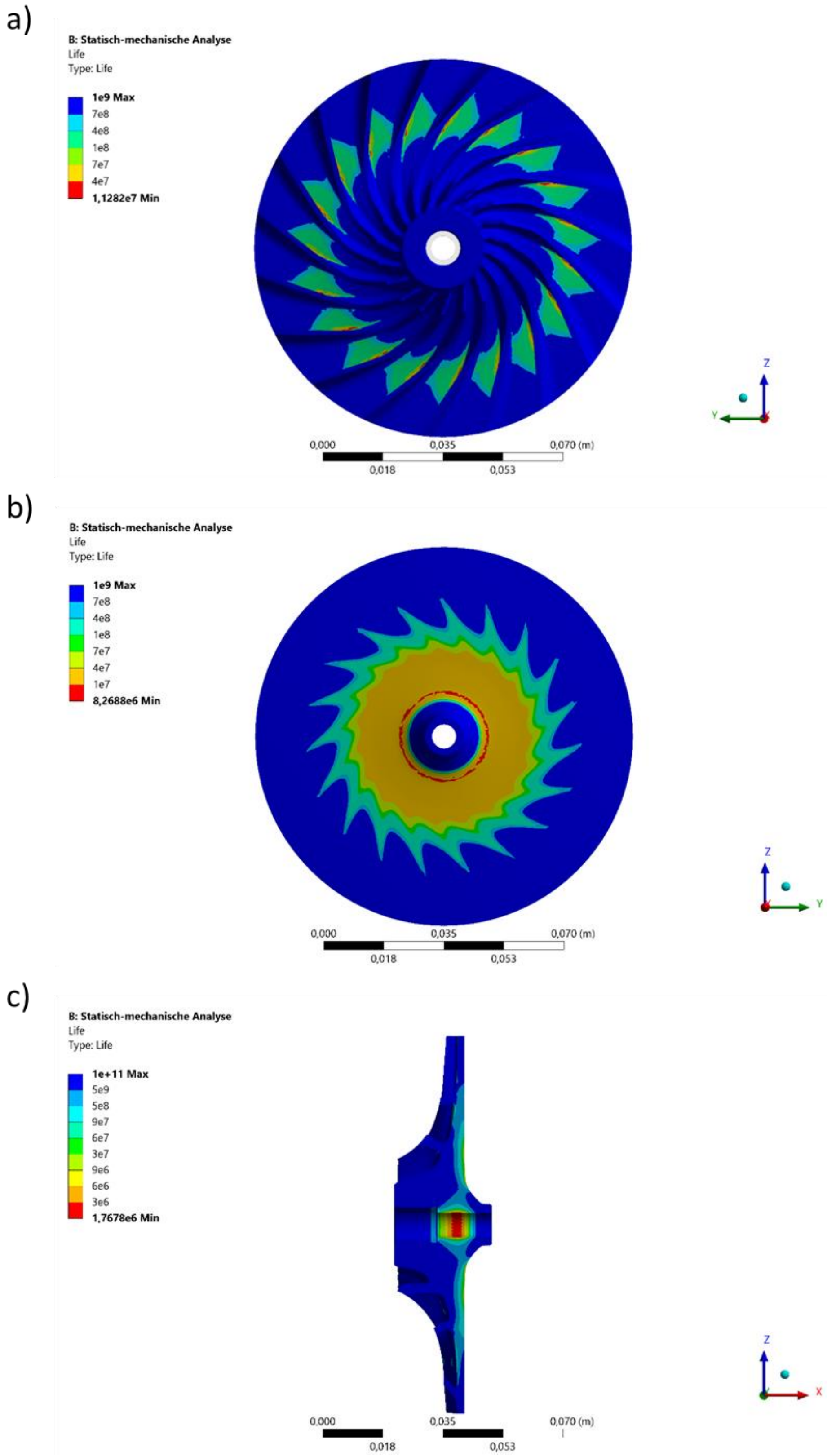

Figure 4-10: Simulated number of cycles to failure of the a) front, b) back, and c) bore region of the impeller

The back of the impeller shows a calculated fatigue life between 3.4e7 and 4e7 cycles to failure on the 19 defined points. The simulation also yields a fatigue life below 4e7 in the same region. The bore region has the highest stress, thus, the lowest number of cycles to failure. The number of cycles to failure for the 19 defined points in this area is between 2.4e6 and 3e5, which is also similar to the simulated fatigue life of below 3e6 cycles in this region. The fatigue life in the three different critical areas is listed in Table 4-2.

Table 4-2: Cycles to failure in the maximum stress points of the three different critical areas of the impeller

Region	Maximum stress (MPa)	Cycles to failure
Front	590	1.1e7
Back	605	8.2e6
Bore	684	1.7e6

The fatigue life of the impeller can be compared to other centrifugal compressors from different studies. Liu et al. [13] assessed the fatigue of a centrifugal compressor made of FV520B steel based on FEA considering aerodynamic load and centrifugal load. They found the fatigue life of their compressor to be between 2.64e7 cycles and 2.13e8 cycles for stress amplitudes between 601 MPa and 490 MPa. Xu et al. [56] also assessed the fatigue life of a remanufactured impeller made of FV520B steel using FEA. Their result showed a fatigue life of 2.37e7 to 2.81e7 for stress amplitudes between 675 MPa and 625 MPa. Reza Kashyzadeh [57] did an FEA study on a centrifugal compressor with the material being a unidirectional fibrous composite and compared it with FV520B steel. They saw that the compressor with the composite material had a fatigue life of 4.2e11 cycles for a maximum von Mises stress of 846 MPa compared to 1.5e7 cycles when the selected material was FV520B. Yakui et al. [58] did an experimental study on the fatigue performance of a compressor blade made of TC6 stainless steel. The fatigue life in the HCF part was found to be in the range of 2.6e7 cycles to 4e7 cycles for a load amplitude between 174 MPa and 112 MPa.

As discussed in section 2.4.2, the HCF and LCF regions of a logarithmic strain-number of cycles to failure plot are described by two different slopes. The HCF part is where there is almost no plastic deformation, whereas there will be plastic deformation in the LCF part of the curve. As seen in the strain analysis of the model, there is almost no plastic deformation in the model. This can be further understood from Figure 4-11, where a logarithmic strain-number of cycles to failure plot is created using the calculated strain and number of cycles to failure. The slope of the fitted line is -0.08, which is close to the slope of -0.09 in the Basquin's equation (for details see section 2.4.3). This further indicates that the strain occurs in the HCF or the elastic region of the S-N curve.

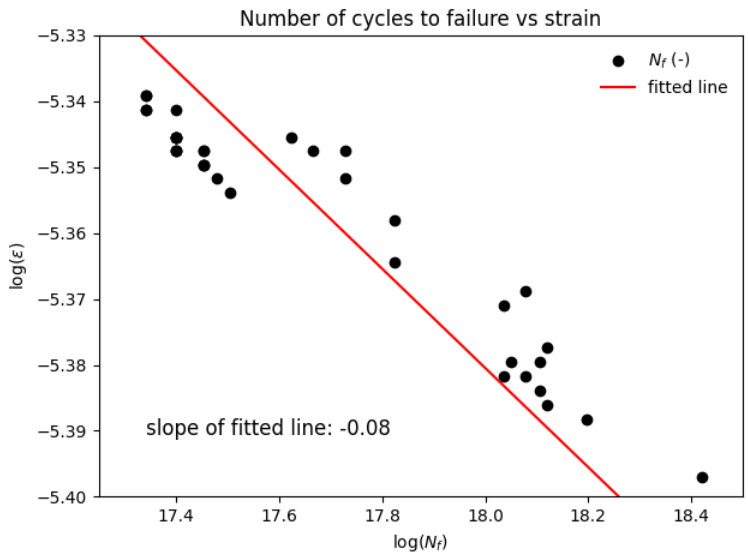

Figure 4-11: logarithmic strain-number of cycles to failure curve

4.3 Vibration analysis

The four natural frequencies observed from the modal analysis in the frequency range of 22500 Hz to 26500 are 22714 Hz, 24480 Hz, 25603 Hz and 25738 Hz. The corresponding mode shapes are shown in Figure 4-12.

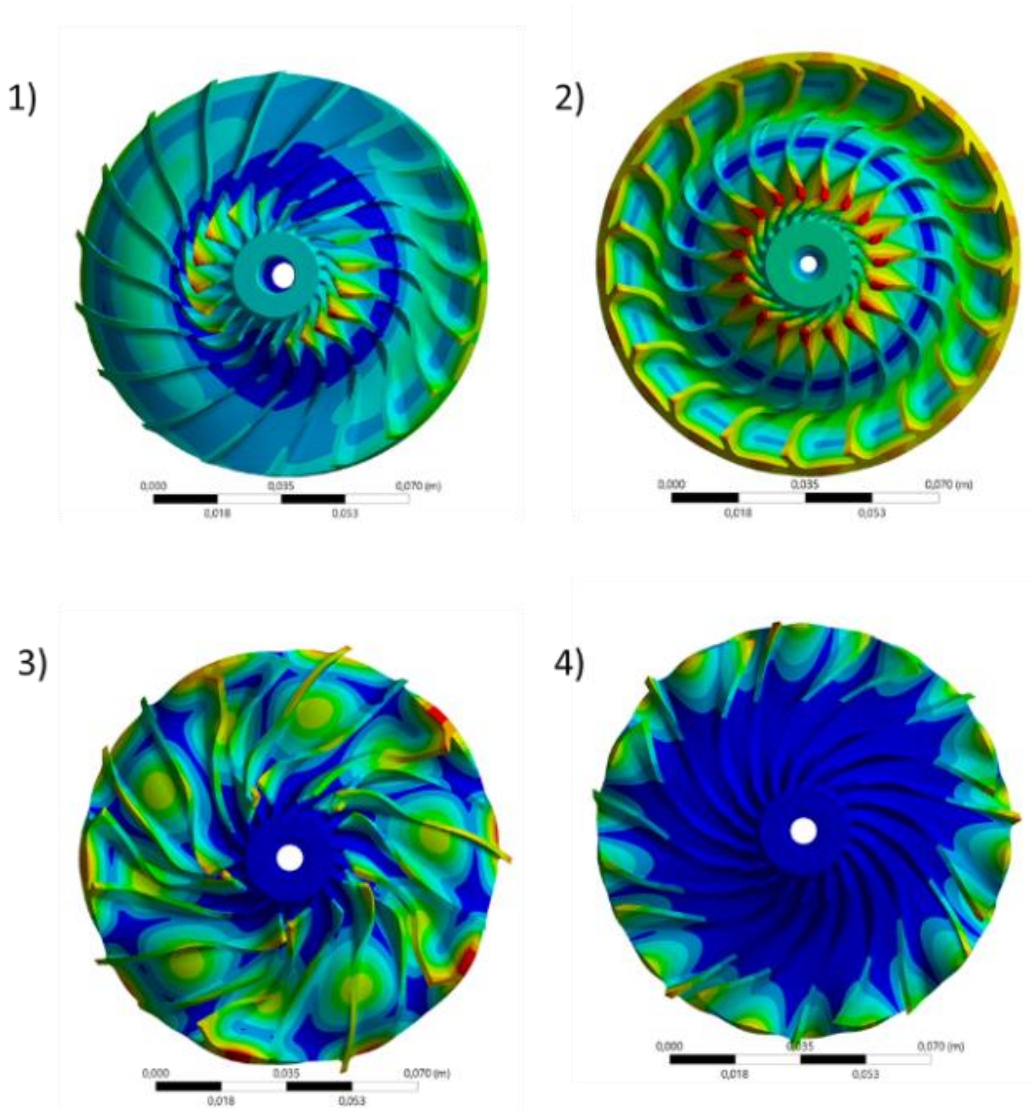

Figure 4-12: mode shapes at the natural frequencies of 1) 22714 Hz, 2) 24480 Hz, 3) 25603 Hz and 4) 25738

From the frequency response analysis, shown in Figure 4-13, a resonance is observed at a frequency of 25600 Hz. As can be seen from Figure 4-12, the mode shape at this natural frequency has 5 nodal diameters.

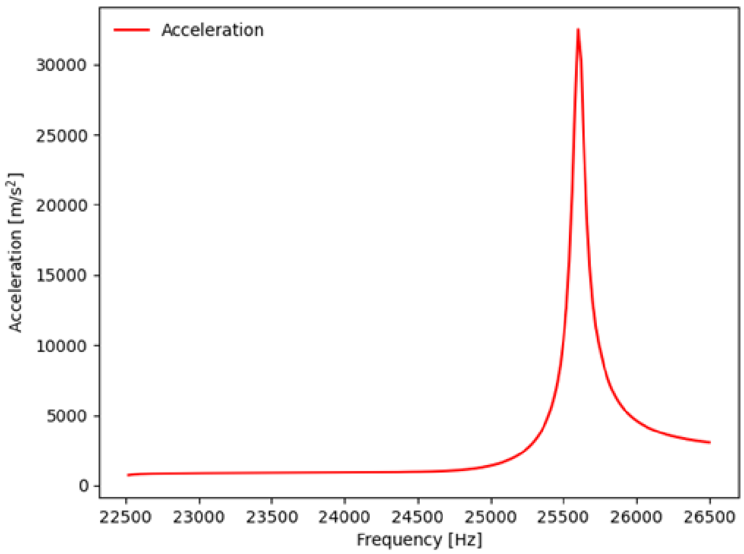

Figure 4-13: Frequency response of the impeller showing resonance at a frequency of 25600 Hz

The theoretical number of nodal diameters of the excited mode shape is determined using the table corresponding to the ZZENF diagram (see equation 2.36 and Figure 2-8). From Table 4-3, it can be seen that for an engine order of 14 and a maximum number of nodal diameters of 9 due to the impeller having 19 blades (see equations 2.33 and 2.34), a mode shape with 5 nodal diameters should be excited, as is seen in the model.

Table 4-3: Number of nodal diameters (ND) for different engine orders with the impeller's engine order marked in red

	$ND = 1$	$ND = 2$	$ND = 3$	$ND = 4$	$ND = 5$	$ND = 6$	$ND = 7$	$ND = 8$	$ND = 9$
$m = 0$	1	2	3	4	5	6	7	8	9
$m = 1$	18	17	16	15	14	13	12	11	10
$m = 1$	18	19	20	21	22	23	24	25	26

The magnitude of the applied forces is increased until the maximum stress on the impeller reaches the yield point of the impeller material. Figure 4-14 shows the stress distribution of the excited mode shape for an applied force of 1 N, 100 N and 1000 N. Since this mode shape occurs at a speed of about 110000 rpm, the stress will be lower when the impeller runs at its full speed of 105000 rpm. The maximum stress occurs on the blades due to the bending and stretching of the impeller. The maximum stress increases linearly with the increase in the applied force. Thus, the observed maximum stress of about 425 MPa at an applied force of 1000 N means that the impeller will reach the material yield strength of 880 MPa at an applied force of about 2000 N.

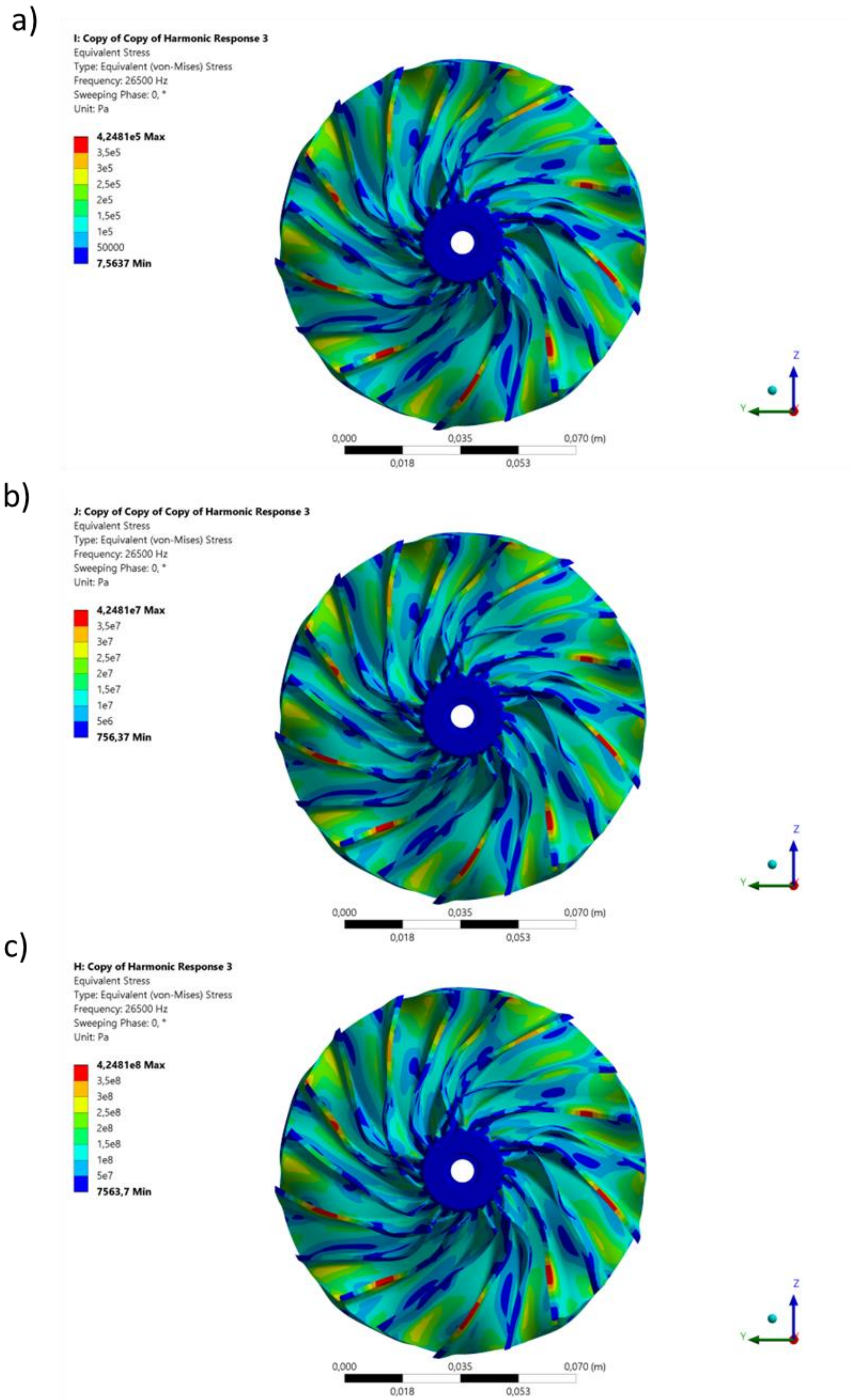

Figure 4-14: Stress distribution of the excited mode shape for applied forces of a) 1 N, b) 100 N and c) 1000 N

The Campbell diagram, shown in Figure 4-15, shows that there is no intersection between the EO14 line and the frequency of the excited mode shape. The maximum operating frequency of 24500 Hz is close to the frequency (25600 Hz) of the excited mode shape. This depicts that the impeller will not have a resonance when operating at 105000 rpm or 24500 Hz. The dominant mode shape, when the impeller operates at full speed, will have 5 nodal diameters.

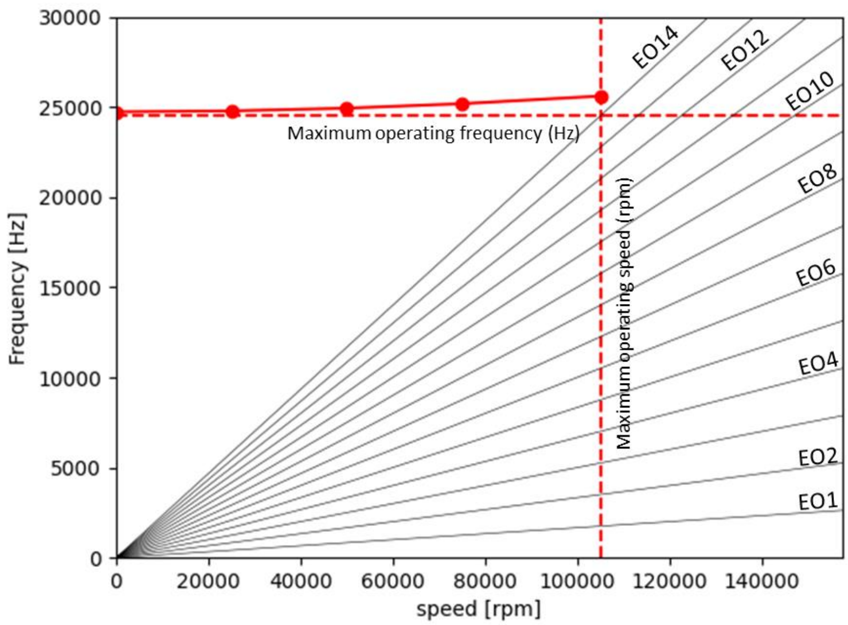

Figure 4-15: Campbell diagram of the impeller with the red markers representing the excited mode shape at different operating speeds and frequencies

5 Conclusion and outlook

One of the vital components of a heat pump system, while also being most prone to failure, is the compressor. Failure of a compressor occurs mostly due to excessive vibration. The lifetime of a compressor is greatly reduced when the compressor runs at its natural frequencies, causing resonance. Furthermore, the compressor is also subjected to alternating cycle load, and dynamic loads, e.g., centrifugal load, aerodynamic load, exciting load, and thermal load. This thesis estimates the service life of a compressor for a high temperature heat pump by performing an FEA on the model of an impeller of a compressor used in a pilot project of the Institute of Low-Carbon Industrial Processes of the German Aerospace Center (DLR) using Ansys Workbench taking into account the compressor’s centrifugal load, pressure load, and thermal load. The geometry of the model included all the parts of the complete assembly of the compressor. This included the impeller, shaft, supports, springs between the shaft and the impeller, lug nut, and bearing regions. The model was solved by assigning the correct materials to each component, doing a mesh study to find the appropriate mesh sizes in the different areas, defining proper contacts and connections, and finally, applying the necessary loads and boundary conditions. The material selected for the impeller was Ti-6Al-4V due to it having a high strength to weight ratio, high operating temperature, high fracture corrosion resistance, and high fracture toughness. The model was also solved using a sector of the full geometry and applying cyclic symmetry to it. However, the bolt pretension due to the pressing of the lug nut onto the springs between the shaft and the impeller could not be properly defined using cyclic symmetry. Furthermore, the stress result in the bore of the impeller also was much lower than expected with the possible reason being the sector model not properly showing the stress due to the interference fit of the impeller onto the shaft. Due to these limitations, the fatigue life of the impeller was calculated using the full geometry. The cyclic life of the impeller was calculated using the so-called Manson-Coffin equation, which relates the total strain amplitude (summation of elastic and plastic strain amplitudes) to the number of cycles to failure. The total strain amplitude was calculated using the Ramberg-Osgood equation. Additionally, a vibration analysis, by means of a modal analysis and a frequency response analysis, was also done to find any resonance and the dominant mode shape at the operating speed of the impeller.

The stress analysis of the model was done based on the von Mises stress criterion. The stress analysis revealed three critical areas on the impeller. The high stress observed on the root of the blades and the disk is a result of the bending stress caused by the rotation of the impeller. Halfway along the length of the blades, another high stress region was observed on the disk. This stress is caused by the bending of the disk itself due to the pressure acting on the impeller. The maximum stress on the front of the impeller was seen where the combined effect of these two stresses was the highest. The high stress on the back of the impeller near the bore region is the result of the high circumferential stress, which can always be seen in annular disks with varying thickness, similar to the geometry of the impeller. The highest stress was observed in the bore region of the impeller. This stress is the result of the circumferential stress caused by the interference fit of the impeller onto the shaft. The simulation yielded maximum stresses of 590 MPa, 605 MPa, and 684 MPa on the front, the back and the bore region respectively. To analyze the stress during one rotation of the impeller, 19 points, due to the impeller having 19 blades, that have the same radial distance from the center and equal angular distances from each other were defined in each of the three critical areas. This method helps to understand the stress a point on the impeller goes through during one revolution of the impeller. The stress values were used to analytically calculate the number of cycles to failure using the Manson-Coffin equation. The fatigue tool in Ansys WB was also used to find the number of cycles to failure. The calculated number of cycles to failure closely matched the simulated values. The minimum number of cycles on the front, the back and the back of the impeller were found to be 1.1e7, 8.2e6 and 1.7e6. This result was then compared to other fatigue life studies done on centrifugal compressors.

The vibration analysis was done by first performing a modal analysis to find the natural frequencies and the associated mode shapes. The engine order of the impeller was identified as 14 as the compressor has 14 diffusor blades. The operating frequency of the impeller, having an engine order of 14 and a rotational speed of 105000 rpm, was calculated to be 24500 Hz. Thus, a harmonic analysis was performed for a frequency range of 22500 rpm to 26500 rpm. Since no transient pressure data was available, imaginary forces were used to perform the harmonic response analysis. The forces were applied tangential to the blades with inter-blade phase differences between them. A resonance peak was observed at a frequency of 25600 Hz, which is higher than the operating frequency of the impeller. Thus, no resonance should be expected when the compressor runs at its full operating speed. The frequency response analysis also showed that the dominant mode shape, when the impeller rotates at its operating speed, has 5 nodal diameters.

The theoretical number of nodal diameters was determined using the ZZENF diagram and was also found to be 5. The magnitude of the force was then increased until the maximum stress observed for the mode shape reached the yield point of the material of the impeller. Finally, a Campbell diagram was drawn to see if there was any crossing between the frequency of the impeller and EO14 line.

While the model is a good representation of the stresses developed in the impeller of the compressor used in this work, it omits several important aspects. Firstly, due to the absence of temperature field data from CFD, the thermal condition was set by assuming a constant temperature for the entire assembly. This is far from ideal since the yield strength of a material is directly related to the temperature. As such, it is not possible to understand which areas of the impeller actually reach the yield point. A properly defined temperature field will also have a direct effect on the stress results. Secondly, no thermal stress analysis was performed on the model. This is also extremely important as the compressor operates at a very high temperature. Thirdly, this work only focuses on the impeller instead of the whole assembly. A static structural simulation should also be done for the whole assembly to understand the stresses in other components, e.g., the shaft, the bearings, and the supports. Finally, while a modal analysis and a harmonic response analysis were done for the impeller, a modal and a rotor dynamic analysis should also be done for the complete impeller-shaft assembly.

Bibliography

1. UNFCCC ADOPTION OF THE PARIS AGREEMENT - Paris Agreement text English
2. International Renewable Energy Agency World Energy Transitions Outlook 2022: 1.5°C Pathway
3. Marina A, Spoelstra S, Zondag HA et al. (2021) An estimation of the European industrial heat pump market potential. Renewable and Sustainable Energy Reviews 139:110545. https://doi.org/10.1016/j.rser.2020.110545
4. Boer R de, Marina A, Zühlsdorf B et al. (2020) Strengthening Industrial Heat Pump Innovation: Decarbonizing Industrial Heat
5. Schlosser F, Jesper M, Vogelsang J et al. (2020) Large-scale heat pumps: Applications, performance, economic feasibility and industrial integration. Renewable and Sustainable Energy Reviews 133:110219. https://doi.org/10.1016/j.rser.2020.110219
6. Birgit Fais, Nagore Sabio, Neil Strachan (2016) The critical role of the industrial sector in reaching long-term emission reduction, energy efficiency and renewable targets. Applied Energy 162:699–712. https://doi.org/10.1016/j.apenergy.2015.10.112
7. J.H. Wesseling, S. Lechtenböhmer, M. Åhman et al. (2017) The transition of energy intensive processing industries towards deep decarbonization: Characteristics and implications for future research. Renewable and Sustainable Energy Reviews 79:1303–1313. https://doi.org/10.1016/j.rser.2017.05.156
8. Kosmadakis G (2019) Estimating the potential of industrial (high-temperature) heat pumps for exploiting waste heat in EU industries. Applied Thermal Engineering 156:287–298. https://doi.org/10.1016/j.applthermaleng.2019.04.082
9. Grassi W (2018) Heat Pumps: Fundamentals and Applications. Springer International Publishing, Cham
10. Roskosch D, Venzik V, Schilling J et al. (2021) Beyond Temperature Glide: The Compressor is Key to Realizing Benefits of Zeotropic Mixtures in Heat Pumps. Energy Tech 9:2000955. https://doi.org/10.1002/ente.202000955
11. Aguilera JJ, Meesenburg W, Ommen T et al. (2022) A review of common faults in large-scale heat pumps. Renewable and Sustainable Energy Reviews 168:112826. https://doi.org/10.1016/j.rser.2022.112826

12. Kim K, Lee YS (2014) Dynamic test and fatigue life evaluation of compressor blades. J MECH SCI TECHNOL 28:4049–4056. https://doi.org/10.1007/s12206-014-0917-5
13. Liu S, Liu C, Hu Y et al. (2016) Fatigue life assessment of centrifugal compressor impeller based on FEA. Engineering Failure Analysis 60:383–390. https://doi.org/10.1016/j.engfailanal.2015.11.035
14. Ashby MF, Shercliff H, Cebon D (2007) Materials: Engineering, science, processing and design, 1. ed. Elsevier, Amsterdam
15. Young WC, Budynas RG, Roark RJ (2002) Roark's formulas for stress and strain, 7th ed. McGraw-Hill, New York, London
16. Pilkey WD (2005) Formulas for stress, strain, and structural matrices, 2nd ed. John Wiley & Sons, Hoboken NJ
17. Budynas RG, Nisbett JK, Shigley JE (2020) Shigley's mechanical engineering design, Eleventh edition. McGraw-Hill Education, New York NY
18. Courtney TH (2000) Mechanical behavior of materials, 2nd ed. Waveland, Long Grove, Illinois
19. Hertzberg RW, Vinci RP, Hertzberg JL (2013) Deformation and fracture mechanics of engineering materials, 5th ed. John Wiley & Sons, Hoboken, N.J., Chichester
20. Callister WD, Rethwisch DG (2010) Materials science and engineering: An introduction, 8th ed. John Wiley & Sons, Hoboken NJ
21. Janeček M, Nový F, Harcuba P et al. (2015) The Very High Cycle Fatigue Behaviour of Ti-6Al-4V Alloy. Acta Phys Pol A 128:497–503. https://doi.org/10.12693/APhysPolA.128.497
22. Rao JS (2000) Turbine blade life estimation. Alpha Science International Ltd, Pangbourne, UK
23. Zhao E, Zhou Q, Qu W et al. (2020) Fatigue Properties Estimation and Life Prediction for Steels under Axial, Torsional, and In-Phase Loading. Advances in Materials Science and Engineering 2020:1–8. https://doi.org/10.1155/2020/8186159
24. U. Muralidharan, S. S. Manson (1988) A Modified Universal Slopes Equation for Estimation of Fatigue Characteristics of Metals. Journal of Engineering Materials and Technology-transactions of The Asme 110:55–58
25. Boller C, Seeger T (1987) Materials data for cyclic loading. Materials Science Monographs, 42B. Elsevier, Amsterdam, Netherlands, New York, New York

26. M.L. Roessle, A. Fatemi (2000) Strain-controlled fatigue properties of steels and some simple approximations. International Journal of Fatigue 22:495–511. https://doi.org/10.1016/S0142-1123(00)00026-8
27. Sharifimehr S, Fatemi A (2019) Evaluation of methods for estimating shear fatigue properties of steels and titanium alloys. International Journal of Fatigue 122:19–34. https://doi.org/10.1016/j.ijfatigue.2018.12.025
28. Dowling NE (2013) Mechanical behavior of materials: Engineering methods for deformation, fracture, and fatigue, 4. ed. Pearson, Boston
29. ASTM International (2023) Standard Terminology Relating to Methods of Mechanical Testing. https://doi.org/10.1520/E0006-23
30. Donaldson BK (2006) Introduction to structural dynamics. Cambridge aerospace series. Cambridge University Press, Cambridge, New York
31. Hauptmann T (2020) Einfluss regenerationsbedingter Varianzen der Schaufelgeometrie auf erzwungene Schwingungen in einer mehrstufigen Turbine, Gottfried Wilhelm Leibniz Universität Hannover
32. Thompson D (2009) Railway noise and vibration: mechanisms, modelling and means of control, 1st. Elsevier
33. Klauke T (2007) Schaufelschwingungen realer integraler Verdichterräder im Hinblick auf Verstimmung und Lokalisierung, Brandenburgischen Technischen Universität Cottbu
34. Murari P. Singh, Bhabesh K. Thakur, William E. Sullivan, George Donald, Singh, Murari P.||Thakur, Bhabesh K.||Sullivan, William E.||Donald, George Resonance Identification For Impellers. https://doi.org/10.21423/R1XM17
35. Srivastava R, Bakhle MA, T.G. K et al. (2004) Aeroelastic analysis of turbomachinery. Int Jnl of Num Meth for HFF 14:366–381. https://doi.org/10.1108/09615530410518002
36. Boyce MP (2012) Rotor Dynamics. In: Gas Turbine Engineering Handbook. Elsevier, pp 215–250
37. Kurowski PM (2004) Finite element analysis for design engineers. SAE International, Warrendale, Pa.
38. Boyer RR (1996) An overview on the use of titanium in the aerospace industry. Materials Science and Engineering: A 213:103–114. https://doi.org/10.1016/0921-5093(96)10233-1

39. Singh P, Pungotra H, Kalsi NS (2017) On the characteristics of titanium alloys for the aircraft applications. Materials Today: Proceedings 4:8971–8982. https://doi.org/10.1016/j.matpr.2017.07.249
40. Rao N (2011) Materials for Gas Turbines – An Overview. In: Benini E (ed) Advances in Gas Turbine Technology. InTech
41. Liu S, Shin YC (2019) Additive manufacturing of Ti6Al4V alloy: A review. Materials & Design 164:107552. https://doi.org/10.1016/j.matdes.2018.107552
42. Rangaswamy P, Choo H, Prime MB et al. (2000) High Temperature Stress Assessment in SCS-6/Ti-6A1-4V Composite Using Neutron Diffraction and Finite Element Modeling. THERMEC 2000 International Conference
43. Ansys Innovation Space. https://forum.ansys.com/forums/topic/need-help-understanding-an-error-in-fatigue-module-2/
44. Liu Z, Zhao H, Zhang C et al. (2023) Investigation on the Evolution of Residual Stress in Ultrasonic Surface Rolling Treatment-Processed 18CrNiMo7-6 Alloy Steel. Trans Indian Inst Met 76:777–785. https://doi.org/10.1007/s12666-022-02776-2
45. Bhadeshia H (2012) Steels for bearings. Progress in Materials Science 57:268–435. https://doi.org/10.1016/j.pmatsci.2011.06.002
46. Richter K, Reuther F, Müller R (2019) A Simulation-Based Approach to Predict the Springback Behavior of Ultra-High Strength Spring Strips. MSF 949:48–56. https://doi.org/10.4028/www.scientific.net/MSF.949.48
47. Chen X, Liu Y (2014) Finite element modeling and simulation with ANSYS Workbench, 1st. CRC Press, Boca Raton
48. Madenci E, Guven I (2015) The Finite Element Method and Applications in Engineering Using ANSYS®. Springer US, Boston, MA
49. Shi D, Xie Y (2020) Aerodynamic Optimization Design of a 150 kW High Performance Supercritical Carbon Dioxide Centrifugal Compressor without a High Speed Requirement. Applied Sciences 10. https://doi.org/10.3390/app10062093
50. Nandi RB, Ghosh P (2012) Centrifugal stress analysis on small cryogenic turboexpander. International Journal of Mechanical Engineering and Research 1:29–33
51. Kienzle NE, Hoang DHM, Waesker M et al. Influence of Fillet Radii on the Flow and Strength Behavior of a Shrouded Centrifugal Compressor Impeller. https://doi.org/10.29008/ETC2021-638

52. Allam MNM, Tantawy R, Yousof A et al. (2017) Elastic and Viscoelastic Stresses of Nonlinear Rotating Functionally Graded Solid and Annular Disks with Gradually Varying Thickness. Archive of Mechanical Engineering 64:423–440. https://doi.org/10.1515/meceng-2017-0025
53. Zenkour AM, Mashat DS (2011) Stress Function of a Rotating Variable-Thickness Annular Disk Using Exact and Numerical Methods. ENG 03:422–430. https://doi.org/10.4236/eng.2011.34048
54. Rotating Machinery Services, Inc. (2021) Engineering Analysis and Structural Tuning of a Centrifugal Compressor Impeller. https://rotatingmachinery.com/analysis-structural-tuning-centrifugal-compressor/#:~:text=When%20an%20impeller%20is%20interference,deformation%20of%20the%20impeller%20bore.
55. Łagodziński J, Kozanecki Z, Tkacz E (2022) Failure Analysis of a Centrifugal Compressor Impeller Made of 17-4PH Steel in the Moist Hydrogen Sulfide Environment. Energies 15:4183. https://doi.org/10.3390/en15124183
56. Xu L, Cao H, Liu H et al. (2016) Assessment of fatigue life of remanufactured impeller based on FEA. Front Mech Eng 11:219–226. https://doi.org/10.1007/s11465-016-0394-x
57. reza kashyzadeh K, Alipanah Kivi S, Rynkovskaya M (2017) Fatigue Life Assessment of Unidirectional Fibrous Composite Centrifugal Compressor Impeller Blades Based on FEA
58. Yakui Z, Shuxiang G (2018) Research on the Fatigue Performance of TC6 Compressor Blade under the CCF Effect. International Journal of Aerospace Engineering 2018:1–10. https://doi.org/10.1155/2018/7154784

Appendix

A Properties of the materials of the compressor components

The materials used in the model are Ti-6l-4V for the impeller, 18CrNiMo7-6 for the shaft, 2007 Aluminum for the lug nut, 100Cr6 for the support 1, 100Cr6 for the bearings, 9SMnPb28K for the support 2, and X10CrNi18-8 for the springs. The mechanical properties of these materials are given in Table A- 1. The fatigue properties of Ti-6Al-4V are calculated. All the other values are obtained from the specifications of the supplier of the compressor.

Table A- 1: Mechanical and fatigue properties of the materials used in the model

Property	Ti-6l-4V	18CrNiMo 7-6	2007 Aluminum	100Cr6	9SMnPb2 8K	X10CrNi1 8-8	Unit
Density	4430	7850	2770	7400	7900	7850	kg/m^3
Coefficient of thermal expansion	9.4e-6	1.2e-5	2.3e-5	1.2e-5	1.2e-5	1.2e-5	1/°C
Modulus of elasticity	1.138e11	2.1e11	7.1e10	2e11	2.1e11	1.865e11	Pa
Bulk modulus	1.2004e11	1.75e11	6.9608e10	1.6667e11	1.75e11	1.5542e11	Pa
Sheer modulus	4.2399e10	8.0769e10	2.6692e10	7.6923e10	8.0769e10	7.1731e10	Pa
Fatigue strength coefficient	1.6445e9	9.2e8	-	9.2e8	9.2e8	9.2e8	Pa
Fatigue strength exponent	-0.09	-0.106	-	-0.106	-0.106	-0.106	-
Fatigue ductility coefficient	0.24872	0.213	-	0.213	0.213	0.213	-
Fatigue ductility exponent	-0.56	-0.47	-	-0.47	-0.47	-0.47	-
Cyclic strength coefficient	9.8425e8	1e9	-	1e9	1e9	1e9	Pa
Strain hardening exponent	0.0345	0.2	-	0.2	0.2	0.2	-
Tensile yield strength	8.8e8	3.35e8	2.4e8	5e8	3.7e8	1.2e9	Pa
Compressive yield strength	9.7e8	3.5e8	3e8	6e8	4.5e8	1.8e9	Pa
Ultimate tensile strength	9.5e8	1.2e9	3.5e8	9e8	4.4e8	1.6e9	Pa
Elongation at break	14	-	-	-	-	-	%
Poisson’s ratio	0.342	0.342	0.33	0.3	0.3	0.3	-

B S-N curves of the materials of the compressor components

The materials used in the model are Ti-6l-4V for the impeller, 18CrNiMo7-6 for the shaft, 2007 Aluminum for the lug nut, 100Cr6 for the support 1, 100Cr6 for the bearings, 9SMnPb28K for the support 2, and X10CrNi18-8 for the springs. The S-N curves of these materials are given in Figure B- 1. The S-N curve of Ti-6Al-4V is plotted using the Palmgren function (equation 2.17). All the other figures are plotted using values obtained from the specifications of the supplier of the compressor.

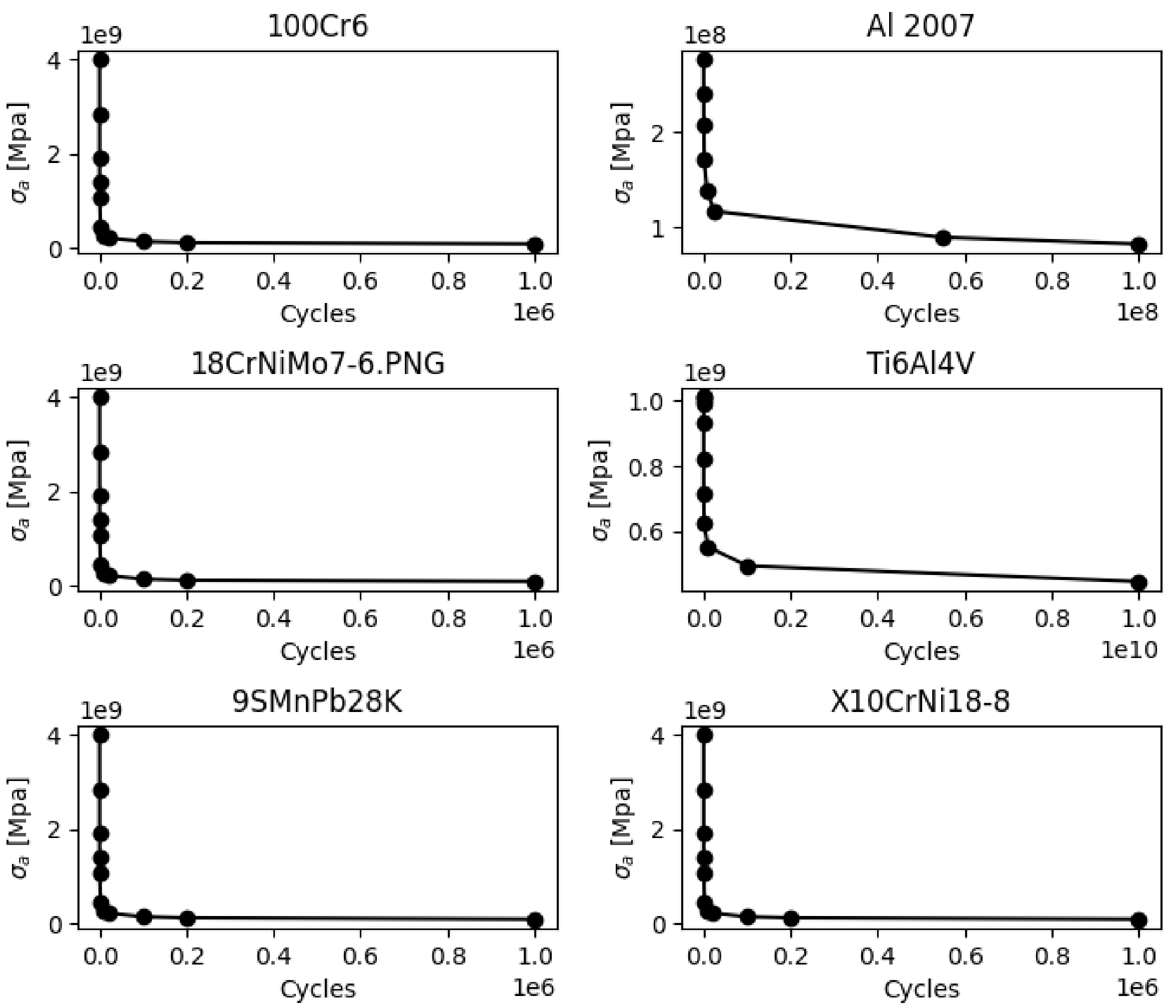

Figure B- 1: S-N curves of the materials assigned to the different components of the FEA model of the compressor

C Mesh study

The element size is considered optimum when the solution shows sufficiently small difference between the averaged and the unaveraged stress results. An averaged stress at a node means the stress value at that nodal point is the average of the stresses calculated for all the elements sharing the node. In an unaveraged result, a node shows all the stresses calculated for the elements the node is shared with. Figure C- 1 shows the stress distribution of the averaged and the unaveraged results. Here, the difference in stresses between the two results is considered sufficiently small to deem the element size as being optimum.

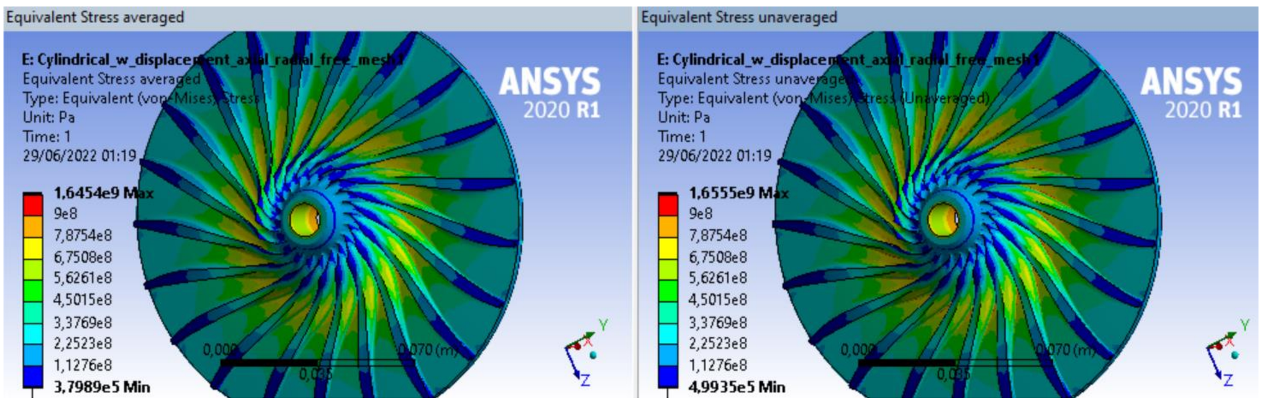

Figure C- 1: Averaged and unaveraged stress distribution of the pre-pilot impeller model